Molecular mechanisms of the asymmetric pit-closing in clathrin-mediated endocytosis

Yiming Yu

Abstract

Clathrin-mediated endocytosis (CME), one of the paramount pathways governing signal transduction between the intracellular environment and extracellular space, has captivated scientific inquiry and sparked debates for over half a century. The application of high-speed atomic force microscopy (HS-AFM) to observe live cell surfaces has unveiled a sequence of morphological transformations of the plasma membrane, including a distinct actin-driven membrane bulge that asymmetrically surrounds the clathrin-coated pit (CCP), resulting in asymmetric pit closing instead of conventional radial constriction. However, the molecular mechanisms underlying this intriguing "asymmetricity" have remained elusive. In this study, I used correlative imaging of HS-AFM and confocal microscopy and superresolution-based techniques to demonstrate that Cdc42-interacting protein 4 (CIP4), a classic Fes/Cip4 homology Bin/amphiphysin/Rvs (F-BAR) domain-containing proteins with structured domains and intrinsically disordered regions (IDRs) is necessary for the asymmetric closing. CIP4 is recruited to the CCP before complete pit closure and further recruits actin-related proteins such as neuronal wiskott-aldrich syndrome protein (N-WASP). Notably, CIP4 undergoes liquid-liquid phase separation (LLPS) and strongly self-assembles via IDRs. Moreover, the condensed phase of CIP4 further concentrates the local G-actin and facilitates actin polymerization, generating an actin-rich microenvironment near the CCP, inducing membrane deformation, and promoting complete pit closure. Overall, this study provides mechanistic insights into the collaborative interplay between disordered and structured domains, shedding light on how they synergistically drive the morphological changes of the plasma membrane and orchestrate spatio-temporal actin polymerization at the closing step of CME.

To my wife and parents

Acknowledgements

Above all else, I would like to convey my most profound appreciation to my supervisor, Dr. Shige Yoshimura, whose invaluable offer allowed me to embark on my PhD journey at Kyoto University and reside in this magnificent city. I am profoundly grateful for his unwavering guidance, steady support, and exceptional mentorship that accompanied me throughout the entire odyssey of my doctoral research. Driven by Dr. Yoshimura's supervision, I received comprehensive training in project conceptualization, experiment design, as well as result analysis and interpretation. It is beyond question that his suggestions, encouragement, and belief in my scientific prowess significantly elevated the calibre of this endeavour.

During my time as a master's student, I acquainted myself with some fundamental experiments in the fields of cell biology and molecular biology. However, since joining Dr. Yoshimura's research group, I have had the privilege of delving into numerous cutting-edge techniques. These include the correlative live-cell imaging of HS-AFM and confocal microscopy, superresolution structural illumination microscopy (SIM), high-performance liquid chromatography (HPLC), and liquid-liquid phase separation (LLPS) assay. Throughout this challenging yet enchanting research journey, Dr. Yoshimura has consistently encouraged me to tackle difficult problems by employing diverse scientific approaches and novel experimental systems. Most notably, he has generously provided me with ample opportunities to do so. I believe this experience will profoundly shape my way of doing science and becoming a true scientist in my future career path.

I would also like to acknowledge all my colleagues at Dr. Yoshimura’s laboratory and researchers outside my lab who greatly support this study for their altruistic technical assistance, constructive discussions, and supportive suggestions. Significantly, Ms. S. Dodo for her expert assistance in the construction of the plasmid; Mr. K. Deguchi for his guidance in the operation of the HS-AFM system; Mr. T. Ozaki for his critical help in the LLPS assay;

Mr. Sakai, Mr. Uekusa, Mr. Yagi, and Mr. Ito for their efforts in the maintenance of the correlative imaging system; Dr. Y. Sasaki at Kyoto University for his valuable suggestions on protein multimerisation; Dr. F. Ishidate at the Institute for Integrated Cell-Material Sciences (WPI-iCeMS), Kyoto University, for his technical assistance in the operation of super-resolution structural illumination microscope (Elyra 7) and, finally, Drs. M. Hijikata, S. Yamashiro, and J. Hejna at Kyoto University, Graduate School of Biostudies, for their practical suggestions on this research. This study heavily relies on their effort for its success.

Finally, I would like to express my most sincere thanks to my parents, who supported me from the very beginning of my research journey and continuously motivating me to strive for greater heights in the realm of science and to my wife Ms. B. Yi who is also my colleague and a doctoral candidate in Dr. Yoshimura's laboratory and one of the bravest and most compassionate people I have ever met in my life. Being an extraordinarily gifted doctoral student, she excelled in her groundbreaking research on anti-HIV host factors and contributed immensely to this study by providing extensive technical support, particularly in plasmid construction, protein purification, and fluorescence microscopic imaging. Together, we have embarked on a journey of science where peaks and valleys mark the path. Yet, we find the most fulfilment in those moments of shared challenges. Therefore, I would like to conclude this section with the following sentiment: "Don't let the water drag you down."

Personal History

Birth:

05/18/1995	HeFei, AnHui Province, China

Education:

9/2010 – 6/2013	HeFei No.10 High School
9/2013 – 6/2017	Undergraduate student at AnHui University, School of Biological Science
10/2017– 5/2019	Master student at Fordham University Graduate School of Art and Science
10/2019 – Present	PhD student at Kyoto University Graduate School of Biostudies

Professional Experience:

10/2017 – 5/2019	Teaching Assistant at Fordham University Graduate School of Art and Science
4/2018 – Present	Teaching Assistant at Kyoto University Graduate School of Biostudies

Professional Affiliation:

4/2020 – Present	Japanese Society of Microscopy

Publications

Original Articles

Yu, Y. & Yoshimura, S. H. Self-assembly of CIP4 drives actin-mediated asymmetric pit-closing in clathrin-mediated endocytosis. *Nat. Commun.* **14**, 4602 (2023).

Reviews and Book chapters

Yu, Y. & Yoshimura, S.H. Investigating the morphological dynamics of the plasma membrane by high-speed atomic force microscopy. *J. Cell Sci.* **134**, jcs243584 (2021).

Presentations and Conferences

1. Yu, Y. & Yoshimura, S.H. (October 5, 2021) "Correlative imaging of high-speed atomic force microscopy and fluorescence microscopy revealed the asymmetric closing process of endocytosis" EMBL Symposium: Seeing is Believing: Imaging the Molecular Processes of Life. [Oral and Poster presentation, **Best Poster Prize**]

2. Yu, Y., Deguchi, K, & Yoshimura, S.H. (May 20, 2020) "Live-cell analysis of protein-mediated membrane deformation during clathrin-mediated endocytosis by High-speed atomic force microscopy" The 76th Annual Meeting of the Japanese Society of Microscopy. [Poster presentation]

Table of Contents

Abbreviation List

CME: clathrin-mediated endocytosis

EGF: epidermal growth factor

LDL: low-density lipoprotein

CCP: clathrin-coated pit

CCV: clathrin-coated vesicle

HS-AFM: high-speed atomic force microscopy

BAR: Bin/amphiphysin/Rvs

F-BAR: Fes/Cip4 homology Bin/amphiphysin/Rvs

IDR: intrinsically disordered region

FDR: flanking disordered region

HR1: G protein-binding homology region 1

SH3: SRC homology 3

Cdc42: cell division control protein 42

Pan1: poly (A)-binding protein-dependent poly (A) ribonuclease 1

Sla1: synthetic lethal with ABP1

End3: endocytosis defective 3

FCHO: F-BAR domain-only protein

Eps15: epidermal growth factor receptor substrate 15

AP2: adaptor protein 2

GUV: giant unilamellar vesicles

CLSM: confocal laser scanning microscopy

PRD: proline-rich domain

PH: pleckstrin homology

HSC70: heat shock cognate protein 70

CLEM: light and electron microscopy

Arp2/3: actin-related protein 2/3

N-WASP: neuronal wiskott-aldrich syndrome protein

FBP17: formin binding protein 17

BIN1: bridging integrator 1

PX: phox homology

APPL1/2: adaptor protein, phosphotyrosine interacting with PH domain and

leucine zipper 1/2

Synd1: syndapin 1

Synd2: syndapin 2

CIP4: Cdc42 interacting protein 4

Toca1:transducer of Cdc42-dependent actin assembly protein 1

GBD: GTPase-binding domain

WIP: WASP interacting protein

GFP: green fluorescent protein

EGFP: enhanced green fluorescent protein

KD: knockdown

FL: full-length

DMEM: Dulbecco's modified Eagle's medium

FBS: fetal bovine serum

SDS-PAGE: sodium dodecyl sulfate-polyacrylamide gel electrophoresis

CLTB: clathrin light chain B

SIM: structural illumination microscopy

PBS: phosphate-buffered saline

Ni-NTA: nickel-nitrilotriacetic acid

GST: glutathione S-transferase

GSH: glutathione

CD: circular dichroism

LLPS: liquid-liquid phase separation

FRAP: fluorescence recovery after photobleaching

BSA: bovine serum albumin

BCA1: bovine carbonic anhydrase 1

Outline of Thesis

Chapter 1 serves as a brief introduction, outlining the fundamental mechanisms of CME from the initiation of the CCP to the maturation and internalization of the CCV and delving into the application of live-cell correlative imaging of HS-AFM and confocal microscopy in investigating the dynamics of the plasma membrane and protein assembly during CME.

Chapter 2 focuses on the morphological characteristics of three distinct closing patterns of the CCP and explores the essential role of CIP4 in the dominant asymmetric closing process, highlighting its significance compared to other F-BAR domain proteins. Furthermore, this chapter also sheds light on the role of FDR in the assembly of CIP4 and how the direct interaction between CIP4 and N-WASP or Cdc42 influences the CIP4 assembly or CCP closing.

In Chapter 3, the study proposes a mechanism elucidating how CIP4 achieves asymmetric assembly through the phase separation of FDR and how the self-assembly of CIP4 contributes to actin polymerization and asymmetric bulge formation.

The final chapter, Chapter 4, provides a comprehensive summary of the main discoveries made throughout this study and discusses how these findings will contribute to our broader comprehension of the endocytic machinery.

Chapter 1: General Introduction

1.1 Clathrin-mediated endocytosis in mammals and yeast

Endocytosis is a cellular event necessary for the transportation of extracellular materials into the cytosol via the deformation of the plasma membrane and the formation of vesicles. The classic endocytic pathway includes phagocytosis, macropinocytosis, clathrin/caveolin-mediated endocytosis, and clathrin/caveolin-independent fast and ultrafast endocytosis (Figure 1-1). Clathrin-mediated endocytosis (CME) is marked by the assembly of a clathrin coat around the vesicle and is responsible for the regulation of a variety of signal transduction pathways and cellular events, including epidermal growth factor (EGF)-dependent cell proliferation, low-density lipoprotein (LDL) uptake, leading-edge formation during cell migration, and integrin-mediated focal adhesion disassembly (Figure 1-1) [1–4]. After half a century of study and investigation, a large proportion of the clathrin-dependent endocytotic machinery has been fully understood, and it is believed that the function and molecular mechanisms of CME are highly conserved in mammals and yeast. For instance, CME in mammalian and yeast cells is composed of a series of morphological changes of the plasma membrane. The membrane is transformed from shallow invaginations to deeply-invaginated narrow or spherical vesicles connecting to the membrane via a tabulated neck [5–7]. Moreover, aside from clathrin and many of its adaptor proteins, which are strictly required for the formation of clathrin-coated vesicles (CCV) in mammals and yeast, actin also plays a critical role in the maturation and transportation of the CCV. In particular, actin filaments flow to the yeast cytosol to assist the clathrin-driven membrane bending, which resulted from the high osmotic pressure pushing the membrane toward the cell wall [8, 9]; In mammals, actin assembles around the CCV before its detachment from the membrane and forms a comet tail attached to the vesicle, which was believed to promote the dynamin-dependent constriction and scission of tubulated membrane and to boost the transportation of vesicles into the cytosol [5]. Regulation of the actin reorganization during CME usually requires the cooperation of

multiple actin-related proteins, such as the poly(A)-binding protein-dependent poly(A) ribonuclease 1 (Pan1), synthetic lethal with ABP1 (Sla1), and endocytosis defective 3 (End3) in yeast and neuronal wiskott-aldrich syndrome protein (N-WASP) and actin-related protein 2/3 (Arp2/3) in mammals [5, 10, 11].

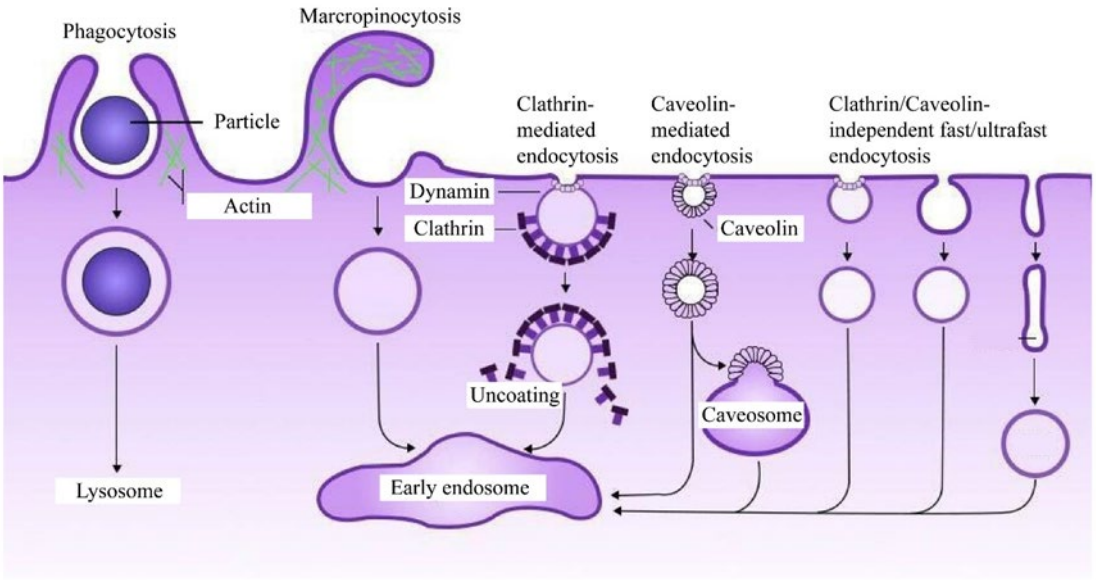

(adapted from geeksforgeeks.org)

Figure 1-1. Endocytosis and clathrin-mediated endocytosis.

Schematic illustrations of classic endocytic pathways, including phagocytosis, macropinocytosis, clathrin/caveolin-mediated endocytosis, and clathrin/caveolin-independent fast and ultrafast endocytosis.

1.2 Clathrin coat assembly and membrane bending

In mammalian cells, the progression of CME involves precise orchestration and sequential recruitment of more than 60 proteins [12]. In the initiation step of CME, multiple adaptors and scaffold proteins were recruited and assembled, including Fes/Cip4 homology Bin/amphiphysin/Rvs (F-BAR) domain-only protein (FCHO), epidermal growth factor receptor substrate 15 (Eps15), adaptor protein 2 (AP2) complex, and intersectin (Figure 1-2)[13–18]. FCHO binds to and curves the phosphatidylserine and phosphoinositides-enriched plasma membrane and interacts with Eps15 and intersectin via the C-terminal mu-homology domain, determining the membranous localization of CME [17, 19]. Eps15 and intersectin recruit AP2 complex, which recruits clathrin to assemble at the membrane into a clathrin coat [20–22].

A single structural unit of the clathrin coat contains three heavy chains and three light chains; each heavy chain interacts with a single light chain, which trimerizes the clathrin molecules (Figure 1-2) [23]. Polymerized clathrin is believed to be the primary driving force of membrane bending by imposing its curvature on the membrane [23]. Membrane bending induced by the clathrin coat is usually accompanied by the increment of membrane tension, which in turn affects the polymerization of clathrin [24, 25]. One vital piece of evidence is that the formation of CCVs was significantly inhibited after hypertonic treatments [24]. Moreover, *in vitro* reconstitution of the membrane invagination process using purified clathrin and adaptor proteins and giant unilamellar vesicles (GUV) revealed that increasing membrane tension could severely impair the polymerization of clathrin [24, 25]. These observations suggested that reshaping of the plasma membrane during CME might remarkably be affected by its physical or biological properties instead of merely responding to the polymerization of clathrin. Based on this understanding, two hotly-debated models have been proposed to explain how clathrin completes the process. One is the ‘constant radius’ model, in which the diameter of the CCP remains constant when the clathrin-coated area keeps growing; the other is called the ‘constant area’ model, in which the clathrin lattice remains flat while the coated area keeps

increasing until it reaches a certain size, then gradually invaginating into a spherical shape [5]. Each of these two models is being supported and challenged by a number of studies. For instance, Dannhauser, P. N. and Ungewickell, E. J. used a cell-free system with a minimum amount of endocytic proteins to simulate the formation and budding of CCVs and pointed out that the polymerization of clathrin alone is sufficient enough to generate deeply-invaginated vesicles which favour the the 'constant radius' model [26]. In good agreement with this, correlative imaging of high-speed atomic force microscopy (HS-AFM) and confocal laser scanning microscopy (CLSM) demonstrated that clathrin kept assembling during the entire invagination process [27].

On the contrary, correlative imaging of light and electron microscopy (CLEM) indicated that the clathrin-coated area remains constant. At the same time, the curvature of CCPs increased, which strongly supports the 'constant area' model [28]. Although more evidence is needed to clarify the machinery of clathrin-dependent membrane bending, a recent study using 3-dimensional superresolution techniques to investigate the geometry of CCPs revealed that clathrin firstly assembled on the flat membrane and covered half of the coated area before the rapid membrane invagination [29]. This finding suggested that the 'constant radius' and 'constant area' models are more likely to be cooperative than mutually exclusive.

1.3 Pit-closing step of CME

From the membrane dynamics perspective, the pit-closing step of CME contains a rapid morphological change of the plasma membrane from shallow U-shaped pits to deeply invaginated Ω-shaped vesicles, and then to the detachment of deeply invaginated vesicles from the plasma membrane, which requires membrane constriction and fission, mainly catalysed by GTPase dynamin (Figure 1-2) [30–32]. Dynamin contains a proline-rich domain (PRD) that binds to the SRC homology 3 (SH3) domain and is recruited to the site of endocytosis mainly by SH3-domain-containing interactors such as members from Bin/amphiphysin/Rvs (BAR) protein families [32], recruited dynamin self-assembles into helical rings surrounding the tubulated membrane, connecting the deeply-invaginated vesicles to the plasma membrane and allowing the constriction of membrane tubule [30]. One theory claims that bending of the pleckstrin homology (PH) domain of dynamin constricts the membrane tubule into a 'hemi-fission' state where the tubule is merely connected with the outer monolayer of the membrane. Then, GTP hydrolysis induces the dynamin disassembly and the tubule's complete scission [32]. Another model suggests that dynamin works as a molecular motor and is powered by several rounds of GTP hydrolysis, leading to the sliding and twisting of the dynamin helix and the membrane scission [32].

Disassembly of the clathrin coat is the last step before the CCV is transported to the cytosol for further processing (Figure 1-2). Heat shock cognate protein 70 (HSC70) is a classic endocytic protein contributing to the uncoating process [33, 34]. HSC70 is connected to clathrin by adaptor proteins auxilin. It promotes clathrin disassembly by either generating steric pressure to attenuate the clathrin-clathrin interaction or disrupting the clathrin lattice owing to its ATPase activity [35, 36]. Besides, accumulating evidence revealed that synaptojanin 1, a polyphosphoinositide phosphatase, and endophilin, a classic BAR domain protein, recycle CCVs [37, 38]. In the neurons of mice with synaptojanin 1 deficiency, accumulated CCVs and increased levels of phosphatidylinositol 4,5-bisphosphate were observed in nerve

terminals [37].

Similarly, the depletion of endophilin in *Drosophila* severely impaired the assembly of synaptic vesicles and induced the formation of densely-coated vesicles [38]. Moreover, endophilin interacts and recruits synaptojanin 1 *in vitro* and *in vivo* [39]. These observations suggested that endophilin cooperates with synaptojanin to promote vesicle uncoating during the late stage of CME.

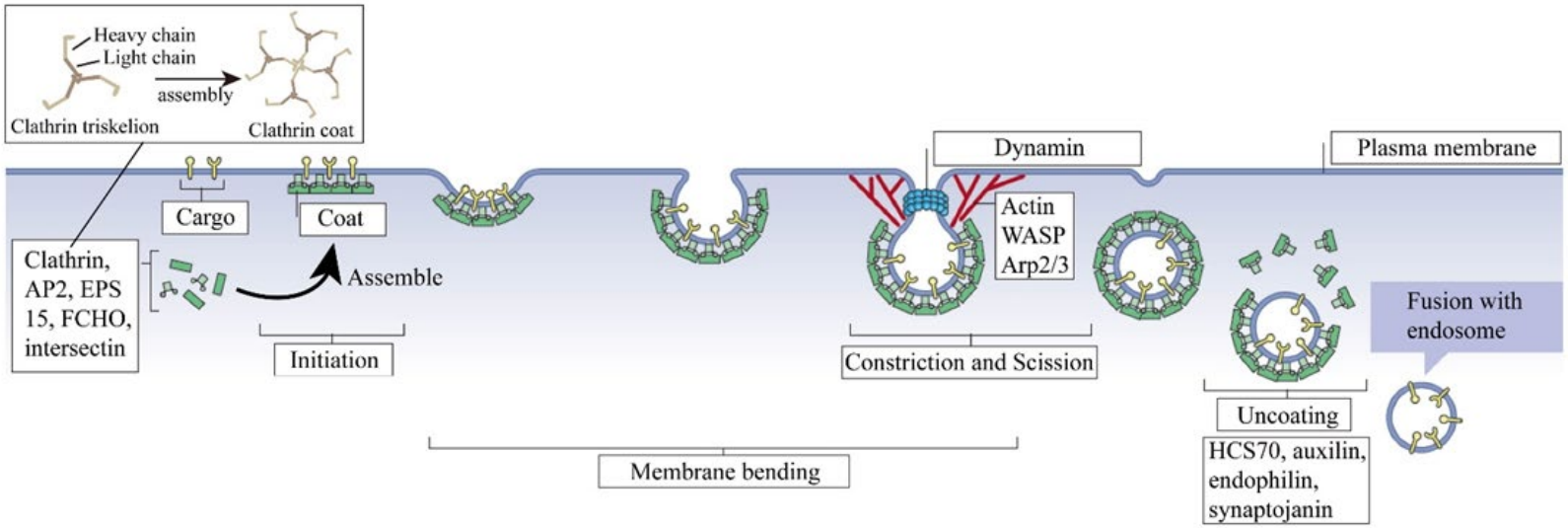

(adapted from Kaksonen and Roux, 2018)

Figure 1-2. Mechanisms of the clathrin-mediated endocytosis.

Schematic illustrations of the progression of clathrin-mediated endocytosis. The initiation step of the clathrin-mediated endocytosis requires the assembly of clathrin, adaptor proteins such as AP2, EPS15, intersectin, and scaffold proteins such as FCHO. These endocytic proteins assemble at the plasma membrane and gradually invaginated the membrane from a U-shaped pit to a Ω-shaped vesicle. The detachment of deeply invaginated vesicles required the constriction and scission mainly driven by dynamin. Matured vesicles were uncoated by HCS70, auxilin, endophilin, and synaptojanin, and were then transported into the cytosol and fused with early endosome for further processing.

1.4 Investigating the molecular mechanisms and membrane morphology at the pit-closing step

The development of super-resolution microscopy has recently led to a groundbreaking revelation regarding the molecular mechanisms underlying the pit-closing step of CME [40–42]. For instance, high-speed superresolution localization microscopy revealed that WASP and myosin recruit Arp2/3-mediated actin polymerization to form two separate actin-enriched zones at the pit-closing step in yeast cells, which drives the vesicle internalization by providing counteractive actin force [40]. Stochastic optical reconstruction microscopy uses photoswitchable probes to label clathrin coat, allowing the 3-dimensional reconstruction of the vesicle structure in 20 to 30 nanometers lateral resolution [41]. One technical obstacle is the determination of the precise closure of the CCP during the live-cell observation, which has posed challenges due to the continued presence of the clathrin coat on the vesicle following its detachment from the plasma membrane. To overcome this hurdle, researchers have successfully identified the moment of CCP closing by labelling CCPs with pH-sensitive fluorescent proteins, specifically the fusion of transferrin receptor with phluorin, and rapidly altering the pH of the external medium between 7.4 and 5.5, and the fluorescence signal can be toggled on and off, allowing for accurate determination of pit closure [43].

Despite the advancements in bioimaging techniques, nanoscale live-cell imaging of the plasma membrane at the pit-closing step remains difficult. The main challenges arise from the limited z-resolution of optical microscopes and the absence of specific fluorescent probes for labelling small membrane structures. However, live-cell HS-AFM imaging has provided a breakthrough for studying the dynamics of a specimen surface, enabling the direct visualization of the entire process of CME, starting from the initial membrane invagination to the final pit closure (Figure 1-3) [27, 44–46]. Additionally, through the implementation of correlative imaging with CLSM, researchers have successfully unveiled the spatiotemporal relationship between protein assembly and pit closure (Figure 1-4) [27]. Notably, in Cos7 cells,

the closure of the clathrin-coated pit occurred ~2 seconds after the peak intensity of dynamin, and the pit closure happened ~3 seconds before the disappearance of the clathrin signal, emphasizing the intricate temporal coordination of these events [27].

Mechanisms of the pit-closing step revealed by correlative imaging of HS-AFM and CLSM deviate significantly from the previously held expectations rooted in the dynamin-driven constriction and scission processes in which the two membranes were brought into proximity followed by a remarkable fusion event between the membranes [47]. In particular, correlative imaging revealed that the knockdown of dynamin only slowed down the constriction process instead of completely aborting the vesicle budding, which agrees with the previous knockout and knockdown experiments involving dynamin 1 and 2. The observation also suggests that dynamin is dispensable for the pit-closing step and strongly indicates the existence of an alternative mechanism responsible for the scission event, challenging the previously established notion of dynamin's essential role in this process [48, 49].

Interestingly, a distinctive membrane protrusion (or membrane bulge) adjacent to the CCP before complete closing has been recently revealed by ion conductance microscopy, and this protrusion gradually expanded and eventually covered the entire pit area [50]. HS-AFM observation of the live Cos7 cell surface later confirmed the presence of membrane bulge during the 'closing phase' characterized by the gradual decline of the clathrin signal (Figure 1-4) [27]. Moreover, correlative imaging of HS-AFM and confocal microscopy using green fluorescent protein (GFP)-fused Lifeact, an actin marker, and CK666, an inhibitor of Arp2/3 complex, demonstrated that the formation of the membrane protrusion is induced by the accumulation of short, branched actin filaments near the CCP (Figure 1-4) [27]. This observation aligns with earlier electron microscope images, indicating the presence of short and branched actin filaments adjacent to CCPs [51]; more importantly, it suggests that when the actin abundancy is high, actin-driven closing may challenge the prevailing dynamin-mediated closing as an individual pathway to promote the complete closure of the CCP.

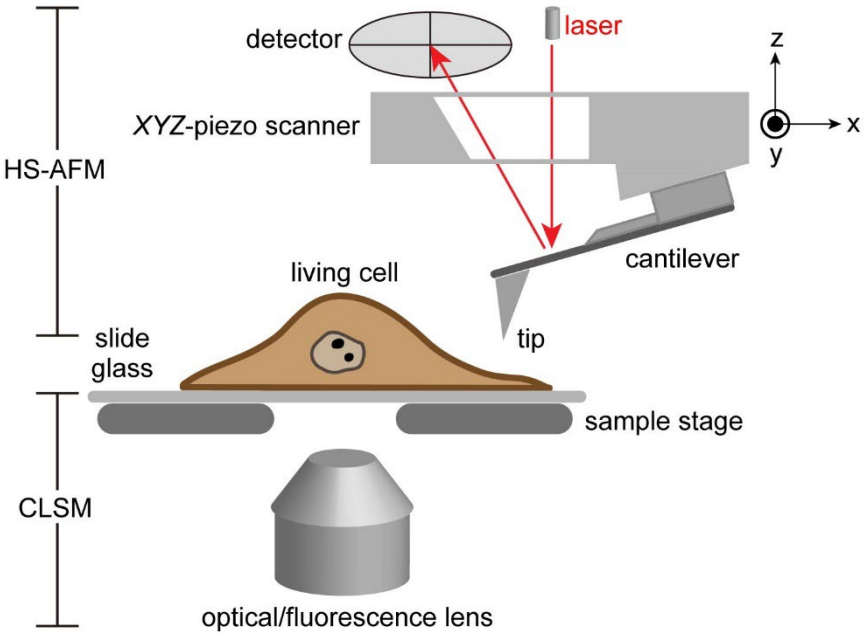

Figure 1-3. Correlative live-cell imaging system of HS-AFM and CLSM.

Schematic illustrations of the live-cell correlative imaging of HS-AFM and CLSM. This system allows the simultaneous observation of protein assembly and membrane dynamics during clathrin-mediated endocytosis.

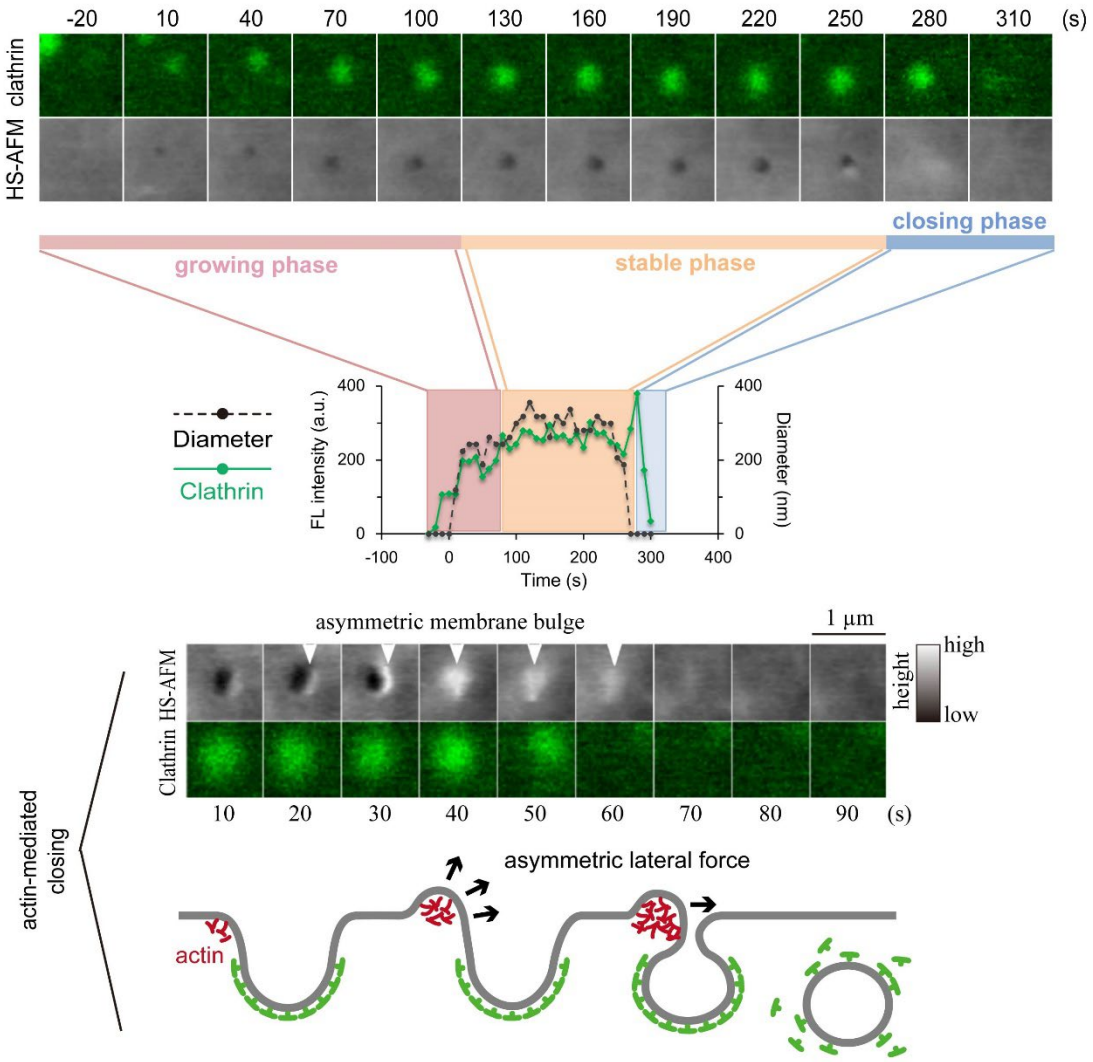

(adapted from Yoshida *et al.*, 2018)

Figure 1-4. Investigate the mechanisms of clathrin-mediated endocytosis by correlative imaging of HS-AFM and CLSM.

The top panel shows an example of clathrin-mediated endocytosis observed by correlative imaging of HS-AFM and CLSM. The fluorescence (FL) intensity of the clathrin signal and the diameter of the clathrin-coated pit were plotted against time. According to the changes in the clathrin signal, the progression of clathrin-mediated endocytosis was separated into growing, stable, and closing phases. Images were taken every 10 s and displayed every 30 s. Images size: 1.0 × 1.0 μm^2. The bottom panel shows the actin-mediated pit-closing process induced by the formation of an asymmetric and actin-driven plasma membrane bulge before the complete closing of the clathrin-coated pit.

1.5 Aim of the study

The primary purpose of this thesis is to demonstrate the detailed underlying molecular mechanisms driving the asymmetric actin assembly and inducing the formation of membrane bulges during the pit closing step of CME. By using the correlative imaging of HS-AFM and CLSM and combining it with multiple cell and molecular biology approaches and biophysical techniques, I investigated the potential role of several F-BAR domain proteins with membrane deformation and actin-association properties in the asymmetric closing process of CME. I hope this study could provide mechanistic insights into how F-BAR domain proteins incorporate actin machinery into CME through the synergistic effect of structured domains and disordered regions.

Chapter 2: CIP4 is necessary for the asymmetric CCP closing

2.1 Introduction

In the first chapter, I described that the membrane bulge drives the asymmetric pit closing merged around the clathrin pit before the formation of deeply invaginated vesicles. This asymmetric membrane protrusion may result from the accumulation of branched actin. Therefore, it is reasonable to assume that upstream regulators of the asymmetric closing should possess two properties simultaneously: the ability to sense or bind to the curved membrane and the ability to recruit or regulate actin signalling around the CCP.

BAR domain-containing proteins are well known as multifunctional regulators of membrane curvature and actin reorganization, making them strong candidates for asymmetric closing [52, 63, 64]. Classic BAR domain proteins such as amphiphysin and bridging integrator 1 (BIN1) contain an N-terminal BAR domain that naturally forms a banana-shaped dimer with various curvatures [53]. Comparison of the amino acid sequence or structural similarities helped to significantly expand the BAR protein family which currently also includes proteins with N-BAR domain (BAR domain with N-terminal amphipathic helix), I-BAR domain (inverted BAR domain), F-BAR domain (BAR with extended Fes/Cip4 homology region), BAR-PH domain (BAR domain with pleckstrin homology domain), and PX-BAR domain (BAR domain with phox homology domain) and forms one of the biggest group of endocytic protein [52].

BAR domain binds to a curved membrane by a dual mechanism. On the one hand, positively charged residues located in the concave surface of dimerized BAR domains bind to negatively charged lipid bilayer and impose the curvature of the dimer to a flat membrane, a mechanism called ‘scaffolding’ [52]. On the other, hydrophobic residues may squeeze into the bilayer and partially insert the BAR scaffold into the membrane, enhancing BAR proteins' membrane-bending abilities [54, 55].

The BAR domain usually undergoes oligomerization to support the bending energy required by endocytosis [52, 56]. For example, phosphotyrosine interacting with PH domain and leucine zipper 1/2 (APPL1/2), adaptors involved in multiple signalling pathways, were reported to form homo- and hetero-multimer via the BAR domain [57]. Similar machinery of self-assembly was also discovered in the F-BAR domain protein family. Syndapin 1 (Synd1), an isoform of Syndapin usually found in neurons, self-associated *in vivo* via F-BAR domain [58]. Disruption of this oligomerization by introducing point mutation impaired the Syndapin 1-mediated actin reorganization and transferrin uptake [58]. Additionally, phase contrast cryo-transmission electron microscopy revealed that the F-BAR dimers of FBP17 or Cdc42 interacting protein 4 (CIP4) are joined end-to-end into filaments and wrap around at the base of CCV and promote the elongation of membrane tubule [59].

Aside from membrane shaping, F-BAR domain proteins are also involved in regulating actin dynamics via the C-terminal SH3 domain. For instance, the transducer of Cdc42-dependent actin assembly protein 1 (TOCA1) was recruited by membrane-bound activated Cdc42 and further recruited N-WASP via the direct interaction between the SH3 domain and the proline-rich region of N-WASP [60]. When recruited N-WASP approach to Cdc42, its N-terminal GTPase-binding domain (GBD) interacts with Cdc42, releasing the C terminal verprolin homology, cofilin homology, and acidic region, which are responsible for initiating Arp2/3-mediated actin polymerization [60]. Moreover, it has been suggested that N-WASP naturally forms complexes with WASP interacting protein (WIP) which inactivate N-WASP and that TOCA1 may indirectly activate N-WASP by suppressing the WIP and destabilizing the N-WASP-WIP complex [61]. Intriguingly, some members of the F-BAR proteins, such as Syndapin 2 (Synd2), a universal isoform of Syndapin, have been reported to interact with actin directly. Synd2 binds to actin filaments via the same concave surface used to bind to membrane [62]. Although accumulating evidence suggests that the F-BAR domain proteins are actively involved in mediating actin dynamics, molecular mechanisms of how F-BAR proteins incorporate actin machinery into CME progression remain elusive and further

studies are required.

2.2 Objective

In this chapter, I will first classify the closing patterns of CCP according to the morphological characteristics of the membrane bulge by analyzing multiple parameters. Then, I will aim to clarify if the F-BAR domain-containing proteins act as the upstream regulators of membrane bulge formation and identify which structured domains or disordered regions play a major in the process. Finally, I will try to illustrate if the F-BAR domain-containing proteins mediate the membrane bulge formation by cooperating with other endocytic proteins or actin-related proteins.

2.3 Results

2.3.1 Asymmetric CCP closing

Under HS-AFM imaging, clathrin-mediated endocytic events were characterized by nearly circular invaginations, ranging in diameter from 150 to 400 nm, with lifetimes spanning from 40 to ~300 seconds [27]. Based on the dynamic processes occurring at the plasma membrane during the closing step of CME, three distinct closing patterns were identified: ‘asymmetric’, ‘symmetric’, and ‘undetermined’ (Figure 2-1A–C). In the asymmetric pattern, a membrane bulge emerged from one side or a specific region of the CCP, gradually covering the pit until complete closure, when the pit's diameter rapidly diminished within 10 to 20 seconds before complete pit closure (Figure 2-1A). The ‘symmetric’ pattern involved a gradual, isotropic shrinking of the pit, eventually leading to complete closure, often accompanied by a subtle membrane bulge (Figure 2-1B). Pits closed within 10 to 20 seconds in a small fraction of cases, yet no discernible bulges were detected even under a higher frame rate (0.5 frames/s) (Figure 2-1C and D). This particular closing pattern was classified as

‘undetermined.’ I found that the frequency of symmetric and undetermined closing is below 20%, while asymmetric closing accounts for ~70% of all closing events (Figure 2-2A), indicating that asymmetric closing is the dominant closing pattern of CME.

The asymmetric bulge exhibited distinct characteristics compared to the symmetric bulge in terms of growth rate (increase in membrane height per unit time), maximum height, and duration (Figure 2-2B). The methods to measure these parameters are described in this chapter's ‘ Materials and Methods’ section. The asymmetric bulge grew faster, achieved greater height, and persisted longer than the symmetric bulge (Figure 2-2B). Furthermore, the closure rate (reduction in diameter per unit time) varied between the asymmetric and symmetric patterns. The asymmetric pattern exhibited a faster closing rate of the pit aperture observed in the HS-AFM images (8.3 ± 3.9 nm/s) compared to the symmetric pattern (3.9 ± 1.8 nm/s) (Figure 2-2B), suggesting that the asymmetric bulge may accelerate the complete closing compared to the symmetric bulge. Despite these differences, CCPs with asymmetric or symmetric closing patterns demonstrated similar total lifetimes (Figure 2-2B), indicating that the closing pattern is not closely related to the overall lifetime of the CCP.

To explore the involvement of actin polymerization in bulge formation, experiments were conducted using CK666, an inhibitor of the Arp2/3 complex, and knockdown (KD) of N-WASP (Figure 2-3A), an upstream activator of Arp2/3. Interestingly, these treatments increased the frequency of pit formation（Figure 2-2A) while significantly reducing the occurrence of asymmetric and symmetric bulges (Figure 2-3B and C), indicating that N-WASP- and Arp2/3-dependent actin polymerization are crucial for the asymmetric closing.

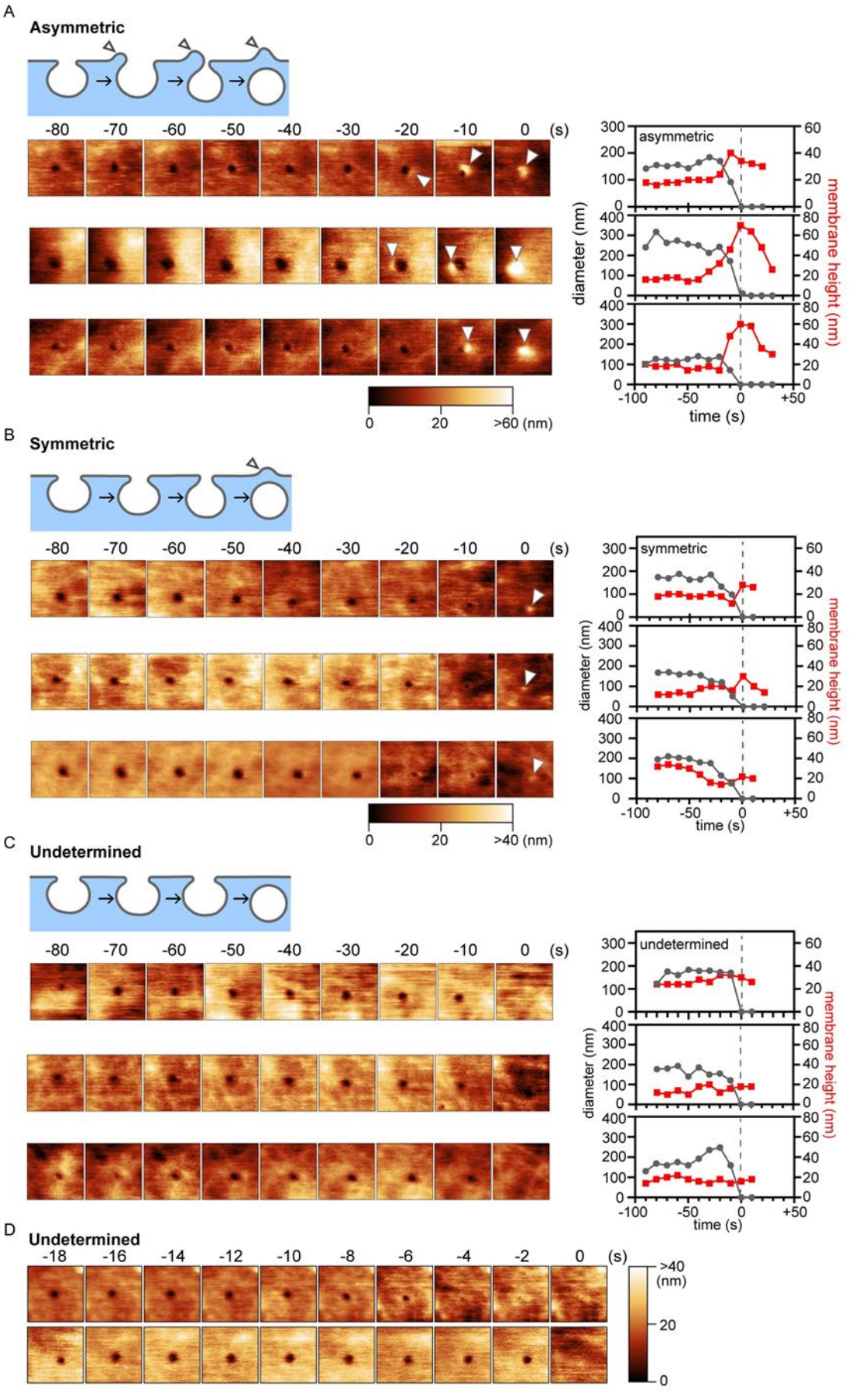
A
Asymmetric
-80 -70 -60 -50 -40 -30 -20 -10 0 (s)
0 20 >60 (nm)
asymmetric
diameter (nm)
membrane height (nm)
time (s)
B
Symmetric
-80 -70 -60 -50 -40 -30 -20 -10 0 (s)
0 20 >40 (nm)
symmetric
diameter (nm)
membrane height (nm)
time (s)
C
Undetermined
-80 -70 -60 -50 -40 -30 -20 -10 0 (s)
undetermined
diameter (nm)
membrane height (nm)
time (s)
D
Undetermined
-18 -16 -14 -12 -10 -8 -6 -4 -2 0 (s)
>40 (nm)
20
0

Figure 2-1. Asymmetric, symmetric, and undetermined closing patterns of the CCP.

A–C, Schematic illustrations and representative time-lapse HS-AFM images of the asymmetric (A), symmetric (B), and undetermined (C) closing patterns of the CCP observed in live Cos7 cells. The frame rate is 0.1 frame/s, and the image size is 1.0 × 1.0 μm^2. The time point when the CCP completely closed on the HS-AFM image is defined as time 0. The position of the membrane bulge is indicated with arrowheads, and the height information of the AFM image is provided using a colour bar. The diameter of CCP (grey) and the maximum membrane height at the pit area (red) are plotted against time for the three distinct closing patterns. The time point corresponding to the complete CCP closure is designated as time 0 and indicated with a black dotted line.

D, Time-lapse HS-AFM images of CCPs with the undetermined closing pattern at a frame rate of 0.5 frame/s. The time point corresponding to the complete CCP closure is designated time 0 and indicated with a black dotted line. The height information of the AFM image is provided using a colour bar. Image size: 1.0 × 1.0 μm^2.

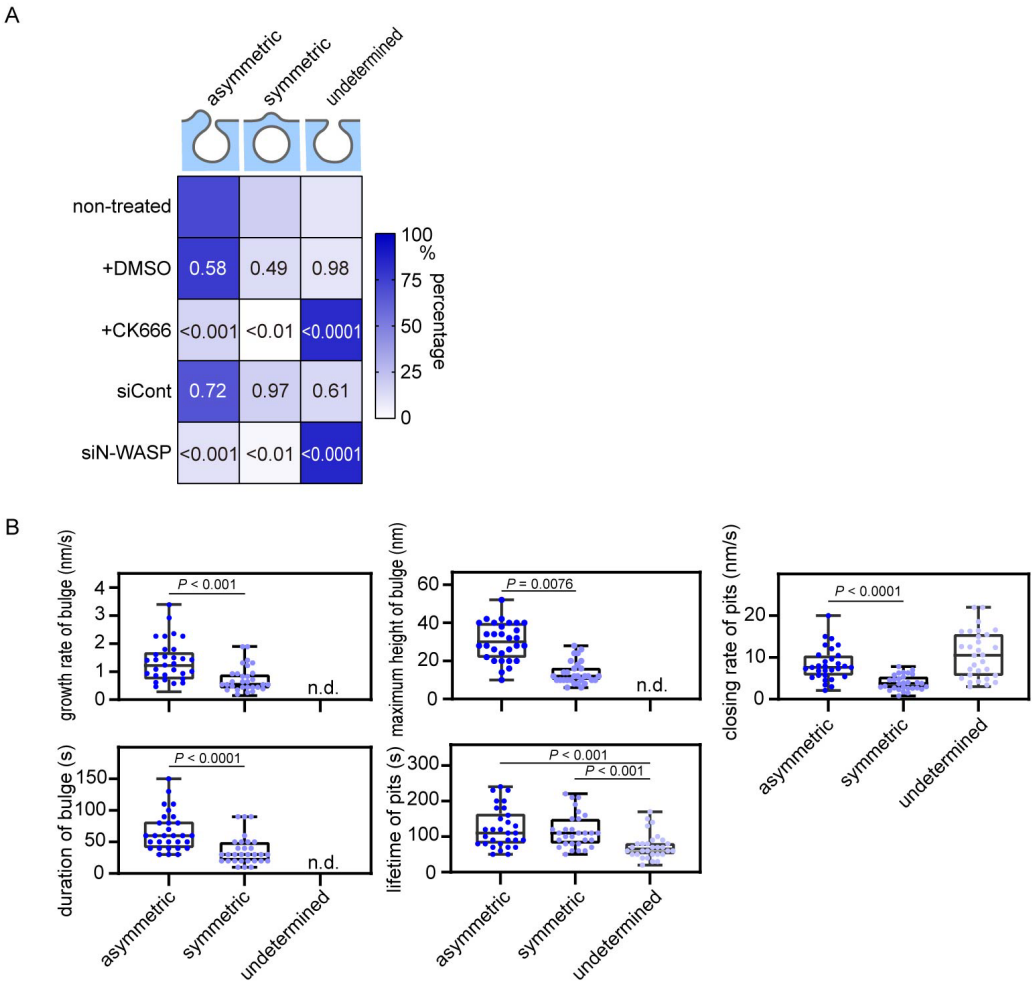

Figure 2-2. The frequency and morphological characteristics of the membrane bulge of the asymmetric, symmetric, and undetermined CCP closing.

A, The heat map illustrates the distribution of three distinct patterns of CCP closing in non-treated Cos7 cells, Cos7 cells treated with DMSO or CK666, and Cos7 cells transfected with control siRNA (luciferase) or siRNA against N-WASP (N = 4 for each condition). The ratio of the same closing pattern between the non-treated and treated groups was compared using a two-tailed Student's t-test, and the corresponding *P* values are indicated in each block. $\alpha = 0.05$.

B, Parameters including the growth rate, maximum height, and duration of the bulge, as well as the total lifetime and closing rate of CCP in each closing pattern, were plotted (N = 30 for each condition). The box plot displays the median, lower and upper quartiles, while the upper and lower whiskers represent the minimum and maximum values. In undetermined cases, the membrane bulge's height, duration, and growth rate were labelled as not defined (n.d.). Statistical analysis was performed using the two-tailed Student's t-test, with $\alpha = 0.05$.

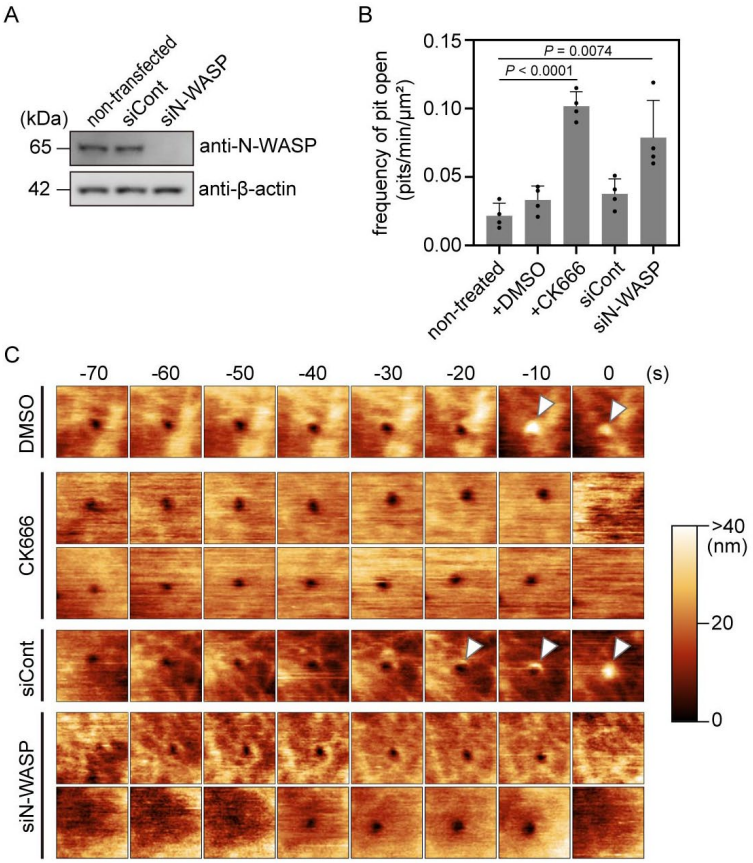

Figure 2-3. Actin polymerization is necessary for asymmetric closing.

A, The knockdown efficiency of N-WASP. The amount of N-WASP in the total cell lysate of non-transfected Cos7 cells and Cos7 cells transfected with siRNA targeting either the control (luciferase) or N-WASP was analysed by immunoblotting using anti-N-WASP antibody. β-actin was used as an internal control.

B, The frequency of CCP formation was summarized in non-treated Cos7 cells, cells treated with DMSO or CK666, and cells transfected with siRNA targeting either the control (luciferase) or N-WASP. The data, represented as mean ± standard deviation, were obtained from four independent experiments, with all data points shown. *P* values were calculated using the two-tailed Student's *t*-test, $\alpha = 0.05$.

C, Time-lapse HS-AFM images obtained from Cos7 cells treated with DMSO or CK666 and cells transfected with control siRNA (luciferase) or siRNA against N-WASP. The time point when the CCP completely closed on the HS-AFM image is defined as time 0. The position of the membrane bulge is indicated with arrowheads, and the height information of the AFM image is provided using a colour bar. Images were taken every 10 s, and the image size is 1.0 × 1.0 μm^2.

2.3.2 CIP4 is necessary for asymmetric bulge formation

As I described previously, I identified the potential role of F-BAR proteins in mediating the asymmetric closing process. All three F-BAR domain proteins localized at CCPs, CIP4, Synd2, and FBP17, were expressed in Cos7 cells (Figure 2-4A and B) [65]. The intracellular concentration of endogenous CIP4 was estimated to be ~20 nM (Figure 2-4C). To analyse the assembly profile of F-BAR domain proteins at the CCP, Cos7 cells co-expressing mCherry-fused CIP4, Synd2, or FBP17 alongside enhanced green fluorescent protein (EGFP)-fused clathrin light chain B (CLTB) were observed by time-lapse fluorescence microscopy (Figure 2-4D–F). CIP4, Synd2, and FBP17 started assembling around the CCP at -26.0 ± 7.4, -16.0 ± 5.5, and -10.5 ± 4.0 seconds, respectively, and disassembled at -5.0 ± 2.3, -7.8 ± 4.4, and -2.0 ± 6.0 seconds, respectively, when the disappearance of the clathrin signal was set as time 0 (Figure 2-4G). KD of CIP4 in Cos7 cells using two siRNA species (one targeting the coding region, siCIP4_coding, and one targeting the 3' untranslated region, siCIP4_3′UTR) resulted in a reduction in the frequency of asymmetric bulges (from ~70% to <30%) and an increase in the undetermined pattern (~70%) (Figure 2-5A–D). Notably, the overexpression of EGFP-fused CIP4 in the CIP4-KD background rescued the occurrence of asymmetric bulges (Figure 2-5C and D). Conversely, KD of Synd2 or FBP17 did not significantly impact any closing patterns (Figure 2-5A, C, and D). In all conditions, the newly formed CCPs' frequency was unaffected (Figure 2-5E). These findings prove that CIP4, but not FBP17 or Synd2, is essential for the asymmetric bulge.

Correlative imaging of HS-AFM and CLSM revealed that the assembly of CIP4 and bulge formation were tightly associated (Figure 2-6A). When the disappearance of the clathrin signal was defined as time 0, CIP4 was detected at -33.9 ± 6.5 seconds under CLSM, while the membrane bulge formed at -30.0 ± 8.2 seconds under HS-AFM (Figure 2-6B). This close temporal relationship strongly suggests a significant correlation between CIP4 and bulge formation.

Observation of the assembly of CIP4 during CME by time-lapse super-resolution structural illumination microscopy (SIM) revealed that the CIP4 signal started appearing at a distinct position offset from clathrin within the initial 5 seconds, with a centre-to-centre distance of 126.8 ± 66.6 nm (N = 160) (Figure 2-6C and D). As the CIP4 signal intensified, the centre-to-centre distance exhibited fluctuations with a gradual decrease until both signals eventually vanished (Figure 2-6C). These observations strongly suggested that CIP4 is asymmetrically assembled around CCP.

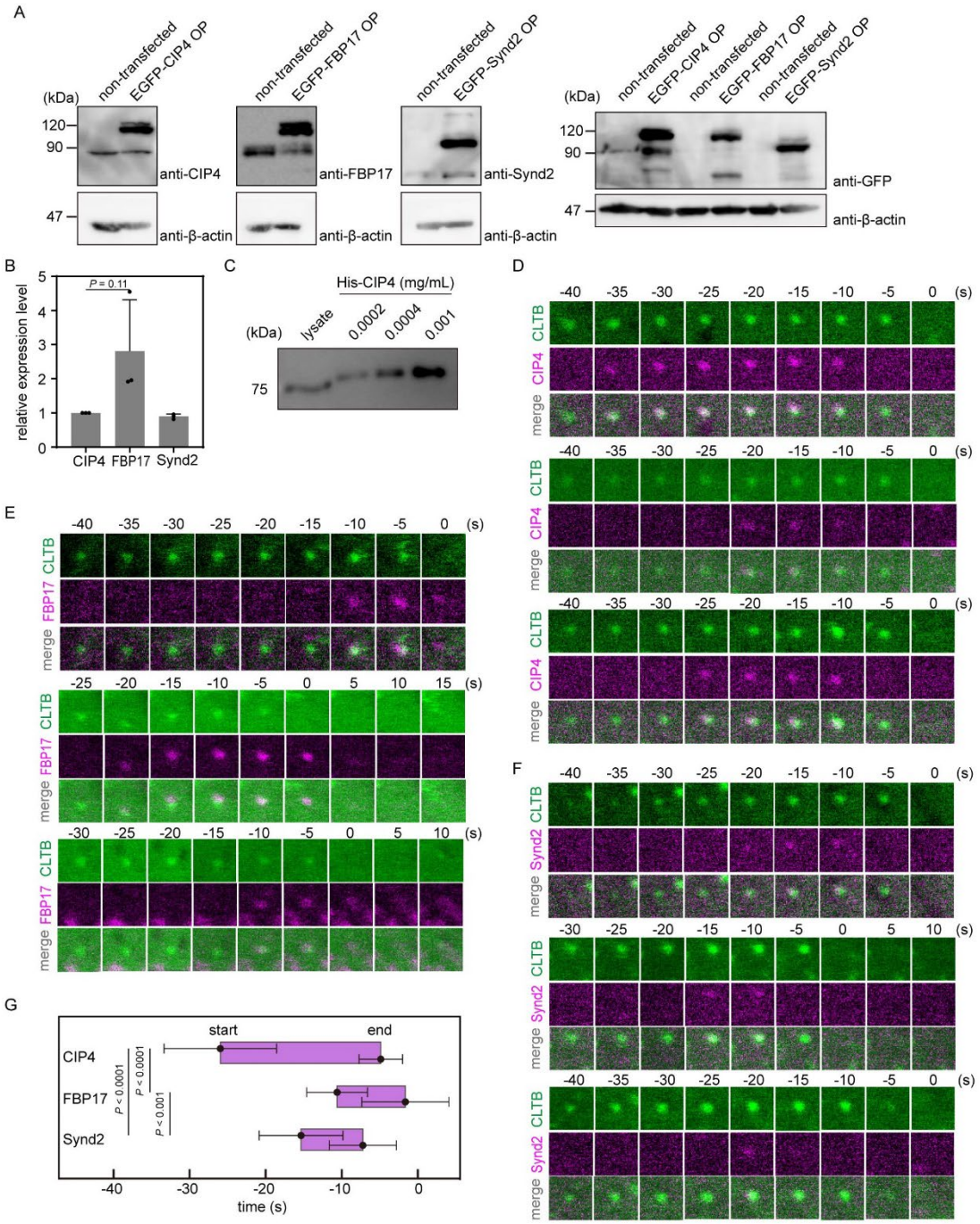

Figure 2-4. Dynamics of CIP4, FBP17, and Synd2 during CME.

A, The cellular level of CIP4, FBP17, and Synd2 in Cos7 cells. The total cell lysate of Cos7 cells expressing EGFP-fused CIP4, FBP17, or Synd2 was analyzed by western blotting using antibodies against CIP4, FBP17, or Synd2, respectively. The same lysate was analyzed using anti-GFP antibody to compare the antibody affinity between anti-CIP4, FBP17, or Synd2 and anti-GFP antibody. Additionally, the amount of β-actin was detected as an internal control.

B, Quantification of the endogenous amount of CIP4, FBP17, and Synd2 analyzed by immunoblotting in (A). Data from three independent experiments were summarized and

presented as mean ± standard deviation. The amount of CIP4 obtained from each experiment is set as ‘1’. All data points are shown, and statistical significance was determined using a two-tailed Student's t-test, $\alpha = 0.05$.

C, The endogenous level of CIP4 in Cos7 cells. The amount of CIP4 in the cell lysate was compared with *in vitro* purified Hexa-histidine-tagged CIP4 with known concentrations by immunoblotting.

D–F, Time-lapse fluorescence images obtained from Cos7 cells co-expressing EGFP-fused CLTB and mCherry-fused CIP4 (D), FBP17 (E), or Synd2 (F). Time 0 was defined as the time point when the clathrin signal of the CCP disappeared. Images size: $1.0 \times 1.0\ \mu m^2$.

G, Summary of the dynamics of F-BAR domain proteins (CIP4, FBP17, and Synd2) at the CCP. The 'start' and 'end' time points, corresponding to the appearance and disappearance of fluorescence signal at the CCP, were recorded and plotted (N = 20 for each condition). Time 0 was defined as the time point when the clathrin signal of the CCP disappeared. *P* values were calculated using the two-tailed Student’s *t*-test, $\alpha = 0.05$. Error bars represent the standard deviation.

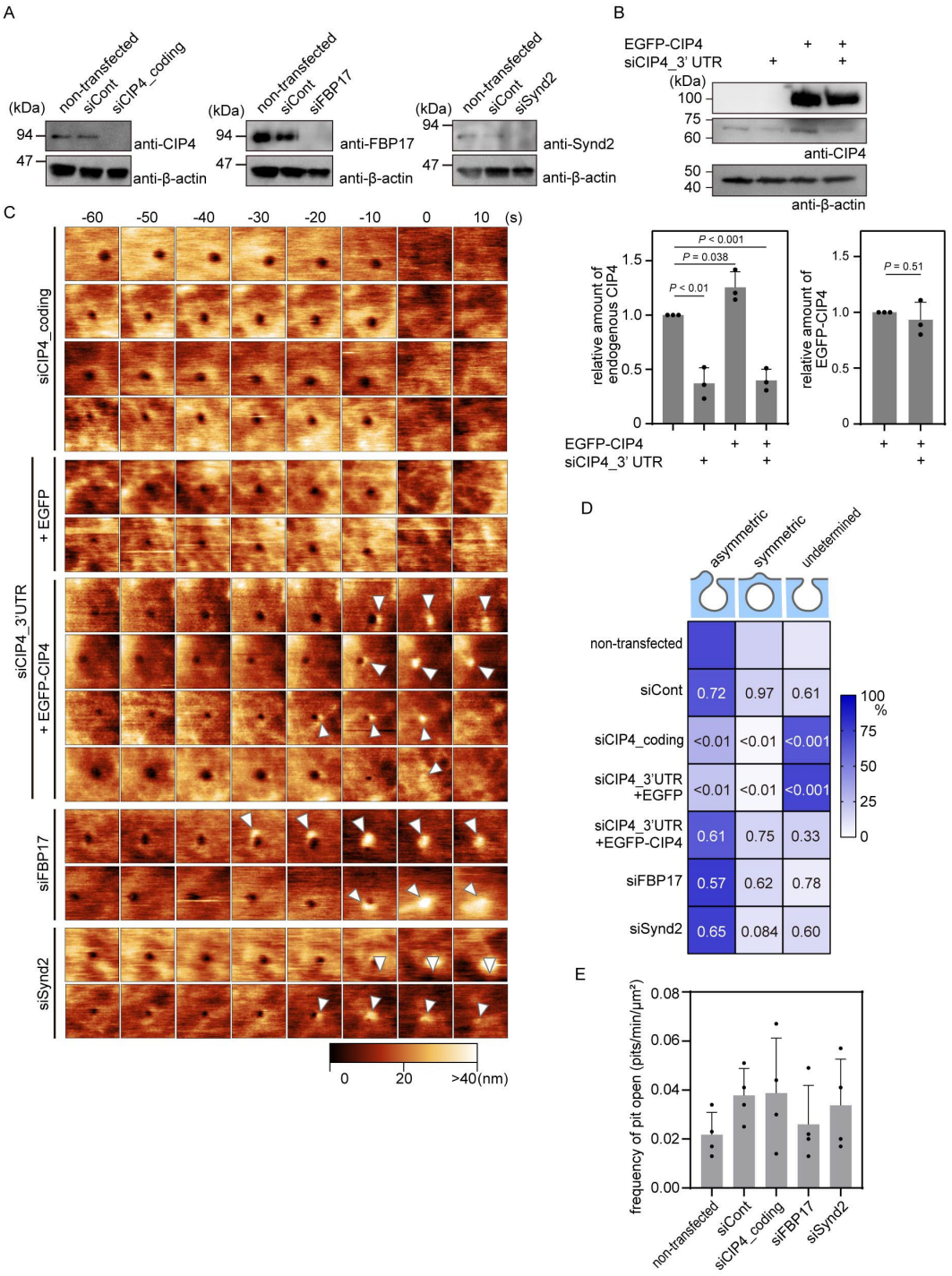

Figure 2-5. CIP4 is necessary for the asymmetric closing.

A, Efficiency of CIP4, FBP17, and Synd2 knockdown by RNA interfering. Total cell lysates from non-transfected Cos7 cells and cells transfected with siRNA targeting the control (luciferase), CIP4, FBP17, or Synd2 were analyzed by immunoblotting using antibodies against CIP4, FBP17, or Synd2. β-actin was used as an internal control.

B, Knockdown efficiency of CIP4 using siRNA targeting the 3′UTR sequence of CIP4

(siCIP4_3′UTR). Total cell lysates were prepared from non-transfected Cos7 cells, cells transfected with siCIP4_3'UTR, and cells transfected with siCIP4_3'UTR followed by transfection of plasmids encoding EGFP or EGFP-fused CIP4. Western blot analysis was performed using anti-CIP4 antibodies, and β-actin was used as an internal control. The relative amounts of endogenous CIP4 and overexpressed EGFP-CIP4 are summarized in the bottom panels. Data from three independent experiments are presented as mean ± standard deviation, and all data points are shown. *P* values were calculated using the two-tailed Student's *t*-test, $\alpha = 0.05$.

C, Time-lapse HS-AFM images obtained from Cos7 cells transfected with siRNA against CIP4 (siCIP4_coding), FBP17, or Synd2 and from Cos7 cells transfected with siRNA against CIP4 (siCIP4_3'UTR) followed by the expression of EGFP or EGFP-fused CIP4. The frame rate is 0.1 frame/s, and the image size is 1.0×1.0 μm^2. The time point when the CCP completely closed on the HS-AFM image is defined as time 0. Arrowheads indicate the position of the membrane bulge, and a colour bar indicates the height information of the AFM image.

D, The frequency of three closing patterns described in (C) was summarized in the heat map. *P* values were calculated by comparing the frequency of the same closing pattern between the non-transfected and transfected group using the two-tailed Student's *t*-test (N = 4 for each condition) and are indicated in each block, $\alpha = 0.05$.

E, The frequency of CCP formation in non-transfected Cos7 cells and Cos7 cells transfected with siRNA for the control (luciferase), CIP4, FBP17, or Synd2 was quantified and is summarised. The results are presented as the mean ± standard deviation derived from four independent experiments, and all data points are displayed. *P* values were calculated using the two-tailed Student's *t*-test, $\alpha = 0.05$. No significant differences were detected between any two groups.

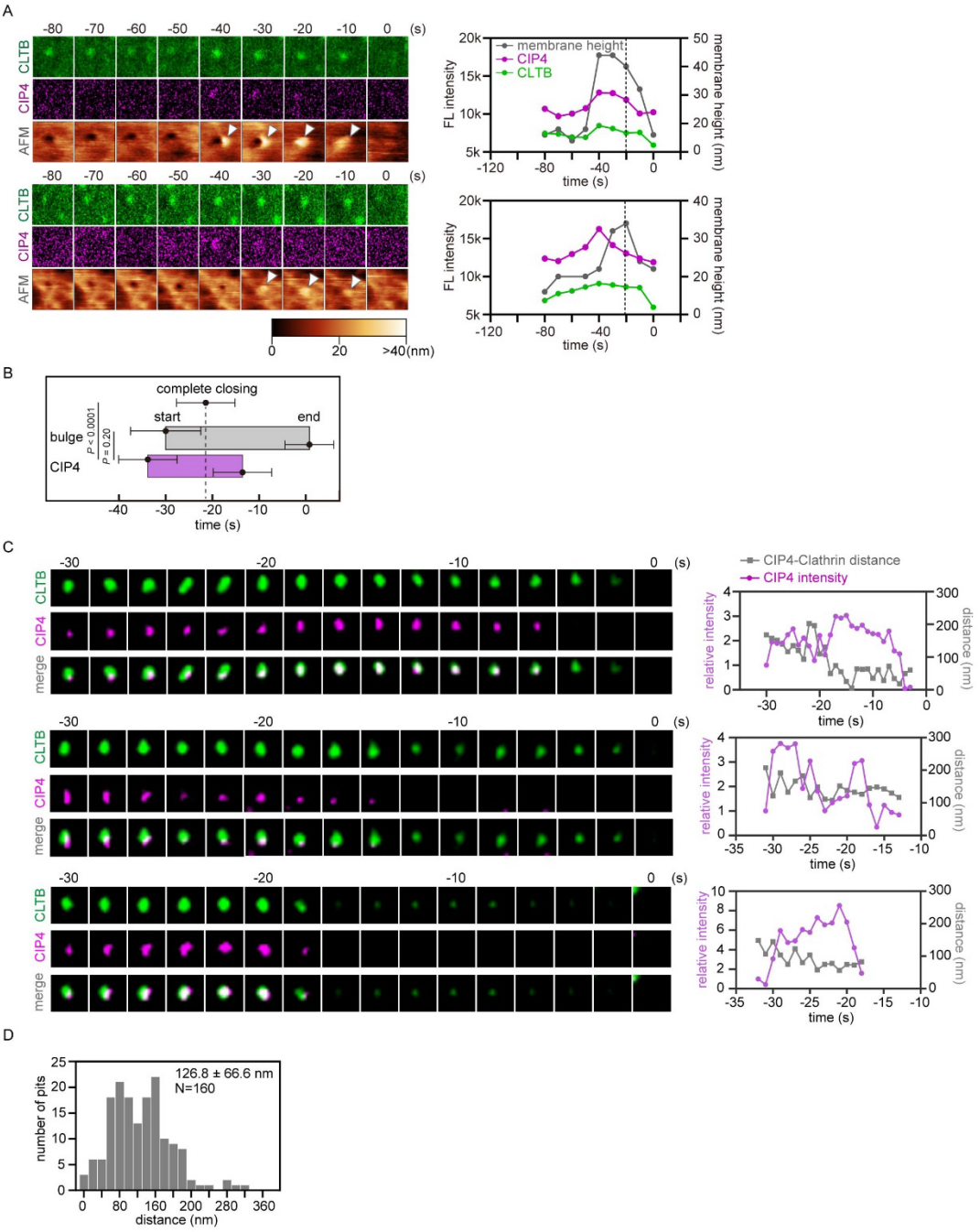

Figure 2-6. CIP4 asymmetrically assembled around CCP.

A, Observation of the CCP by correlative imaging of HS-AFM and CLSM. Images were acquired every 10 s from Cos7 cells expressing EGFP-fused CLTB and mCherry-fused CIP4. Image size: 1.0 × 1.0 μm². Time 0 was defined as the moment when the clathrin signal disappeared. Arrowheads indicate the position of the membrane bulge, while a colour bar presents the height information of the AFM image.

B, Summary of the dynamics of CIP4 and membrane bulge observed by correlative imaging.

The time points of membrane bulge formation and disappearance and the appearance and disappearance of the CIP4 signal at the CCP area were designated as the ‘start’ and ‘end’ time points, respectively, and were plotted (N=16). *P* values were calculated using the two-tailed Student’s *t*-test, $\alpha = 0.05$. Error bars represent the standard deviation.

C, Time-lapse observation of Cos7 cells expressing EGFP-fused CLTB and mCherry-fused CIP4 by super-resolution SIM imaging. Images were taken every second and displayed every 2 s. Image size: 0.5×0.5 μm^2. Time 0 was defined as the time point when the clathrin signal of the CCP disappeared. The fluorescence intensity of CIP4 and the x-y distance between the centroids of clathrin and CIP4 are plotted against time (bottom).

D, The centre-to-centre distance between the centroids of the CIP4 and clathrin signal observed by fluorescence imaging within the first 5 s of CIP4 assembly was summarized in a histogram (N = 160, from 32 CMEs).

2.3.3 Flanking disordered region is pivotal for CIP4 assembly at CCP

Subsequently, the specific domains of CIP4 required for its assembly around the CCP were identified. CIP4 and FBP17 are members of the F-BAR protein subfamily and possess conserved F-BAR and SH3 domains at their amino- and carboxyl-termini, respectively (Figure 2-7A–C). The amino acid sequence between F-BAR and SH3 domains is predominantly disordered and less conserved (Figure 2-7A–C). In the case of CIP4 and FBP17, but not Synd2, the middle-disordered region is interrupted by a conserved G protein-binding homology region 1 (HR1) and is therefore named flanking disordered region (FDR).

The assembly of CIP4 at the CCP remained unaffected by the deletion of the SH3 domain (CIP4(ΔSH3)) (Figure 2-7A and 2-8A). When separately expressed, neither the F-BAR domain nor the FDR assembled at the CCP because the signal dots indicating the assembly of these two fragments were almost unobservable (N = 20) (Figure 2-7A and 2-8B). These observations demonstrate that both the F-BAR domain and the FDR are necessary for CIP4 assembly, while the SH3 domain is not required for this process. Interestingly, chimeric molecules carrying the Synd2-BAR and CIP4-FDR (referred to as SCC and SC chimaeras in Figure 2-7A) assembled at the CCP at a similar time point to that of the full-length CIP4 instead of Synd2 (Figure 2-8C–E), the CS chimaera, which carried the CIP4-BAR and Synd2-IDR (Figure 2-7A), failed to assemble at the CCP (N = 20) (Figure 2-8F). Thus, these findings demonstrate that aside from the F-BAR domain, the FDR of CIP4 also plays a significant role in its assembly at the CCP.

A

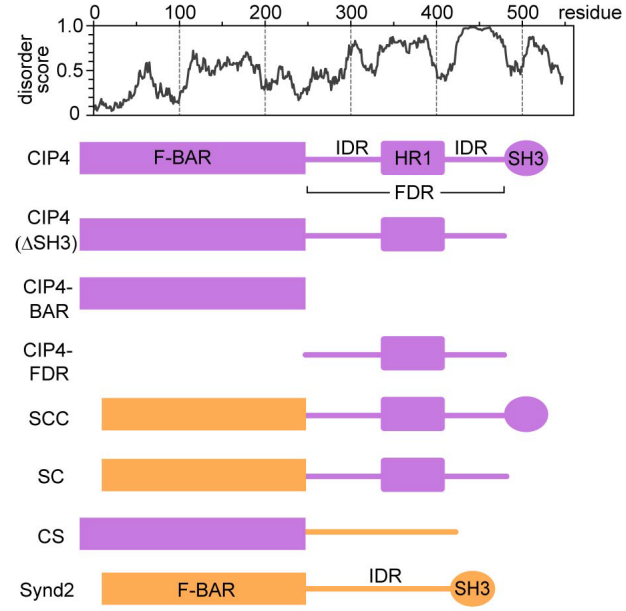

C

similarity (%) domain / domain	CIP4-F-BAR
FBP17-F-BAR	79.4
Synd2-F-BAR	39.3

similarity (%) domain / domain	CIP4-SH3
FBP17-SH3	70.8
Synd2-SH3	46.7

similarity (%) domain / domain	CIP4-FDR
FBP17-FDR	52.6
Synd2-IDR	13.8

B

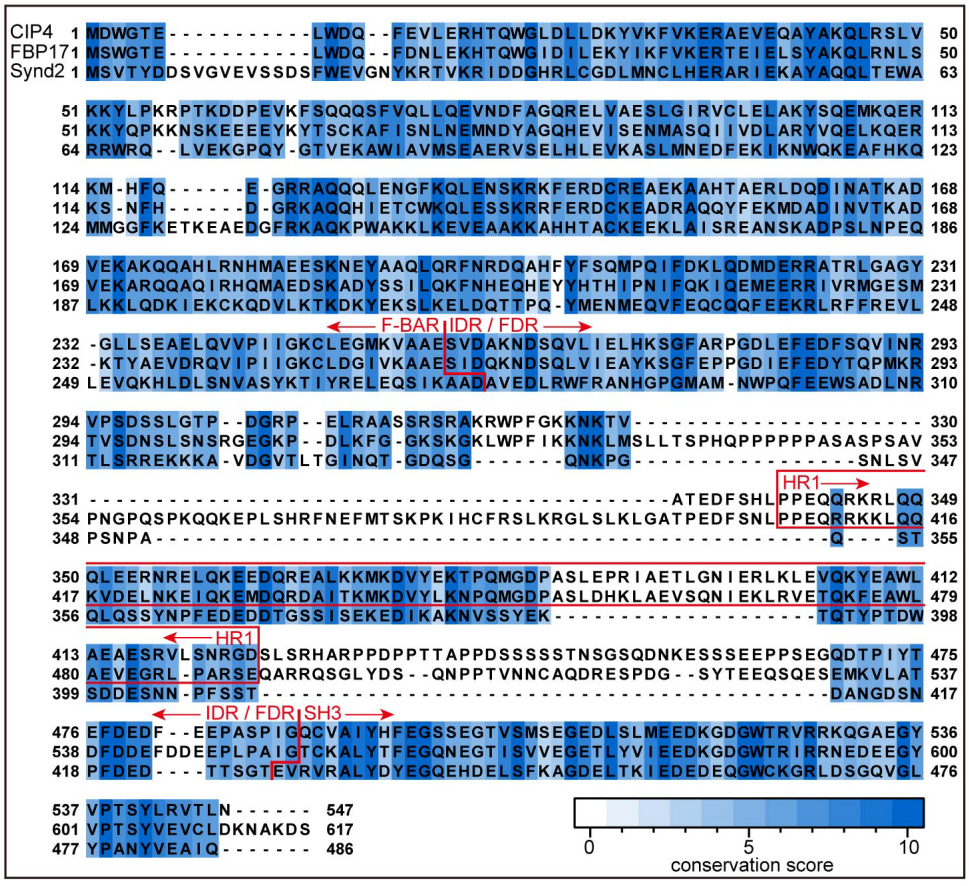

Figure 2-7. Comparison of the domain structure and amino acids similarities among CIP4, FBP17, and Synd2.

A, (Top) Disorder plot of CIP4. (Bottom) Schematic illustration of the domain structures of CIP4, Synd2, CIP4(ΔSH3), CIP4-F-BAR, CIP4-FDR, and chimeric molecules (SCC, SC, and CS).

B, Multiple amino acid sequence alignment using *Mus musculus* CIP4 (Uniprot, Q8CJ53-3), *Homo sapiens* FBP17 (Uniprot, Q96RU3), and *Mus musculus* Synd2 (Uniprot, Q9WVE8). The structured domains and disordered regions were labelled, and the conservation score was indicated in a colour bar.

C, Similarities of the F-BAR, SH3, and FDR/IDR among CIP4, FBP17, and Synd2.

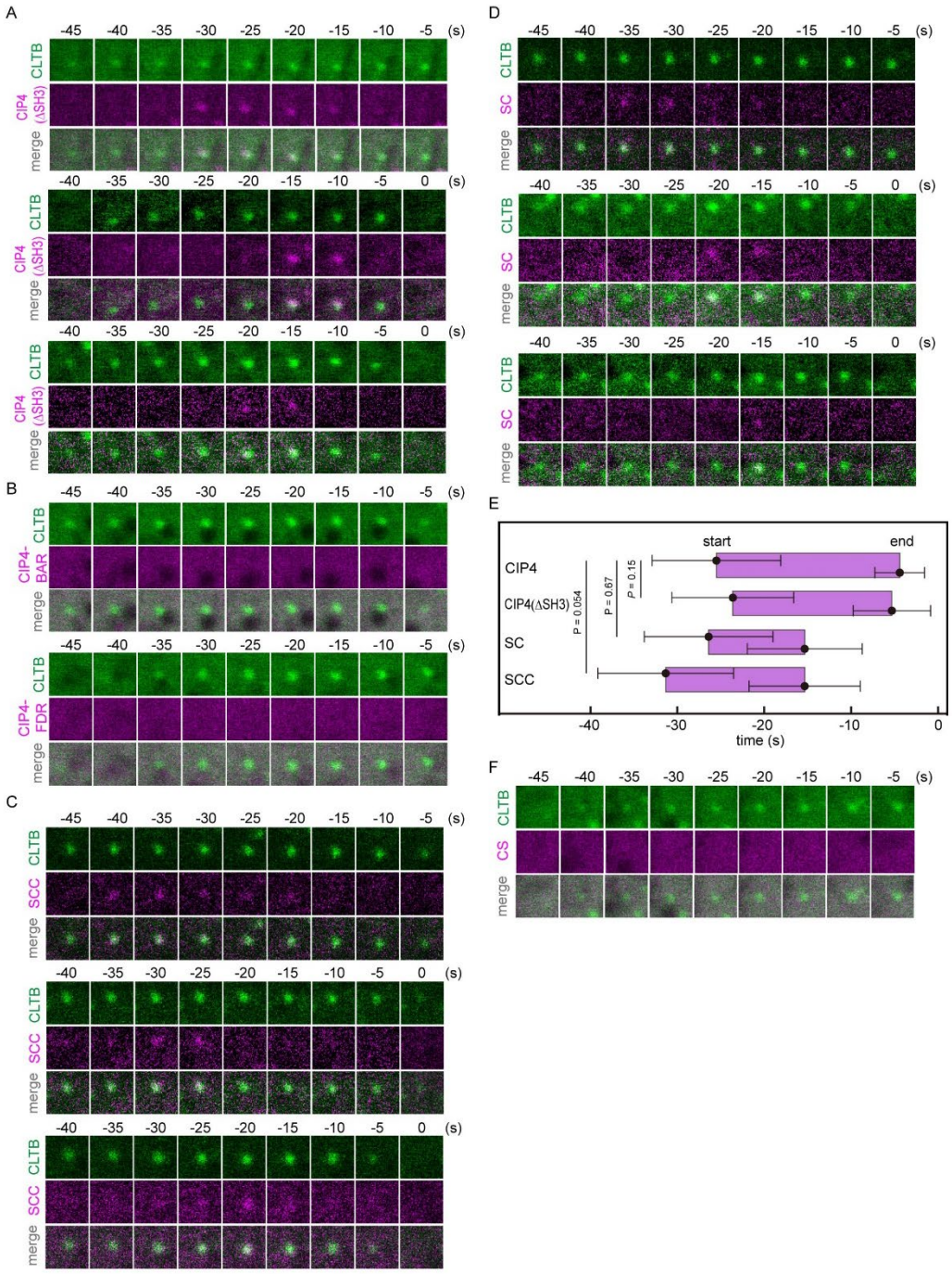

Figure 2-8. FDR mediates the assembly of CIP4.

A–D and F, Time-lapse fluorescence images obtained from Cos7 cells co-expressing EGFP-fused CLTB and mCherry-fused CIP4(ΔSH3), F-BAR, FDR, or chimeric molecules (SCC, SC, and CS). The image size is 1.0 × 1.0 μm^2. The time point when the clathrin signal disappeared is defined as 0.

E, A summary of the dynamics of CIP4, CIP4(ΔSH3), and chimeric molecules at CCP. The time point when the clathrin signal disappeared is defined as 0. The timing when the

fluorescence signal appeared and disappeared at the CCP area was determined as ‘start’ and ‘end’, respectively, and are plotted (N = 20 for each condition). *P* values were calculated using the two-tailed Student’s *t*-test, $\alpha = 0.05$. The error bars represent the standard deviation.

2.3.4 SH3 domain is required for membrane bulge formation

Although the SH3 domain is dispensable for the assembly of CIP4, further investigation revealed that the expression of the SC chimeric molecule, which assembled at the CCP, was unable to rescue the CIP4-KD phenotype, and the frequency of the asymmetric closing remained unrecovered by the expression of the SC chimaera (Figure 2-9A). In contrast, the SCC chimeric molecule, which contains the SH3 domain of CIP4, could rescue the KD phenotype (Figure 2-9A). These observations suggested that the SH3 domain is critical for asymmetric bulge formation.

CIP4 is known to interact with activate N-WASP through its SH3 domain (Figure 2-9B) [66]. Activated N-WASP further interacts with Cdc42 via its GBD and recruits the Arp2/3 complex to facilitate actin polymerization (Figure 2-9C) [67]. In our study, I observed N-WASP assembly at the CCP, occurring immediately after CIP4 assembly (Figure 2-9D). Hence, I investigated whether the interaction between CIP4 and N-WASP was crucial for forming the asymmetric bulge. Introducing a point mutation (W518K) in the SH3 domain of Toca1 was reported to hinder its interaction with N-WASP [61]. Similarly, mutating the corresponding residue (W524K) in the CIP4-SH3 domain reduced its interaction with N-WASP (Figure 2-9B). Consistent with these findings, the SCC chimeric molecule carrying the W524K mutation failed to rescue the CIP4-KD phenotype (Figure 2-9A), indicating that the interaction between CIP4-SH3 and N-WASP is indispensable for the formation of the asymmetric bulge.

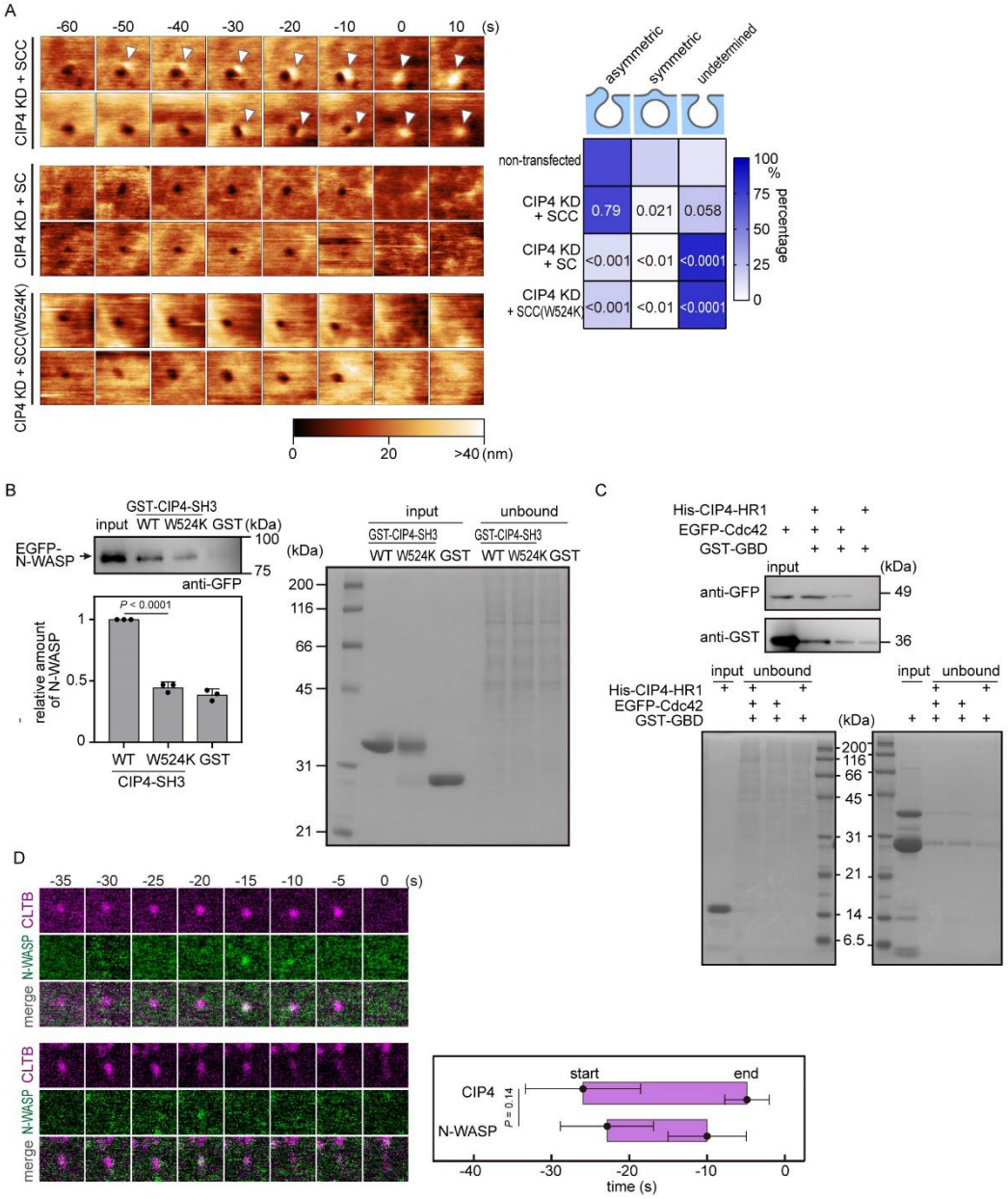

Figure 2-9. SH3 domain is necessary for asymmetric bulge formation.

A, Time-lapse HS-AFM images obtained from Cos7 cells depleted of CIP4 by RNA interfering followed by the transfection of plasmids encoding EGFP-fused SCC, SC, or SCC(W524K) mutants. The frame rate is 0.1 frame/s, and the image size is 1.0 × 1.0 μm^2. The time point when the clathrin signal disappeared is defined as 0. The position of the membrane bulge is indicated with arrowheads, and the height information of the AFM image is provided using a colour bar. The frequency of three closing patterns was measured and summarised in the right panel (N = 4 for each condition).

B, The interaction between GST-tagged CIP4-SH3 (WT) or CIP4-SH3 (W524) and EGFP-

fused N-WASP was examined using a pull-down assay. HeLa cell lysate containing EGFP-fused N-WASP was mixed with GSH beads bound to GST-tagged CIP4-SH3 (WT or mutants). The eluted fractions were subjected to western blotting using the anti-GFP antibody (left top). The resulting immunoreactive bands were quantified and summarized (left bottom). The data, presented as mean ± standard deviation from three independent experiments relative to the WT variant, are displayed with all data points shown. *P* values were calculated using the two-tailed Student's t-test, $\alpha = 0.05$. Additionally, the input amounts of GST-tagged CIP4-SH3 (WT), CIP4-SH3 (W524K), empty GST, and the unbound fraction from the pull-down assay were analyzed using SDS-PAGE (right).

C, Pull-down assay among CIP4-HR1, Cdc42, and the GBD of N-WASP. GST-tagged GBD was first incubated with or without hexahistidine-tagged CIP4-HR1, then with the cell lysate containing EGFP-fused Cdc42. The eluted fractions were analyzed using western blotting with the anti-GFP antibody (top). Additionally, the input amount of CIP4-HR1 and the unbound fraction were analyzed using SDS-PAGE (bottom).

D, (top) Time-lapse fluorescence images of EGFP-fused N-WASP and mCherry-fused CLTB co-expressed in Cos7 cells. Time 0 was defined as the time point when the clathrin signal of the CCP disappeared. The image size is $1.0 \times 1.0\ \mu m^2$. (bottom) Summary of the dynamics of CIP4 and N-WASP at the CCP. Time 0 was defined as the time point when the clathrin signal of the CCP disappeared. The timing when the fluorescence signal appeared and disappeared at the CCP area was defined as ‘start’ and ‘end’, respectively, and are plotted as mean ± standard deviation (N = 20, for each condition). *P* values were calculated using the two-tailed Student’s t-test, $\alpha = 0.05$.

2.3.5 Cdc42 recruits CIP4 to the CCP

My investigation explored the involvement of the FDR in the asymmetric assembly of CIP4. Specifically, CIP4 is known to interact with activated (GTP-loaded) Cdc42 via its middle region [68]. Pull-down assay revealed that the CIP4-FDR exhibited a more vital ability to bind to the active form of Cdc42 (loaded with GTPγS) compared to the FBP17-FDR and the IDR of Synd2 (Figure 2-10A and B). Moreover, by substituting three amino acids located in the HR1 (M381I, G382S, and D383T, in Figure 2-10C), which are known to disrupt the Cdc42 interaction with Toca1 [67], the interaction between CIP4-FDR and Cdc42 was also impaired (Figure 2-10A and B). Notably, the assembly of CIP4(IST) mutants at the CCP initiated at -12.5 ± 5.2 s, displaying a delayed onset compared to the wild-type (WT) CIP4 assembly (Figure 2-11A and B). These findings suggest that activated Cdc42 is necessary for CIP4 assembly at the CCP.

Moreover, the interaction between Cdc42 and CIP4 proves crucial for CIP4 assembly and the formation of the asymmetric bulge. Notably, overexpressing a dominant-negative form of Cdc42 (T17N) significantly impaired the asymmetric bulge formation (to ~25%) compared to non-transfected cells (Figure 2-11C). Conversely, the overexpression of WT Cdc42 did not yield the same effect (Figure 2-11C). Furthermore, the SCC(IST) mutants failed to rescue the CIP4-KD phenotype (Figure 2-11C). These observations suggest that the assembly of CIP4 at the CCP, which further induces the asymmetric bulge, is mediated by the activated Cdc42.

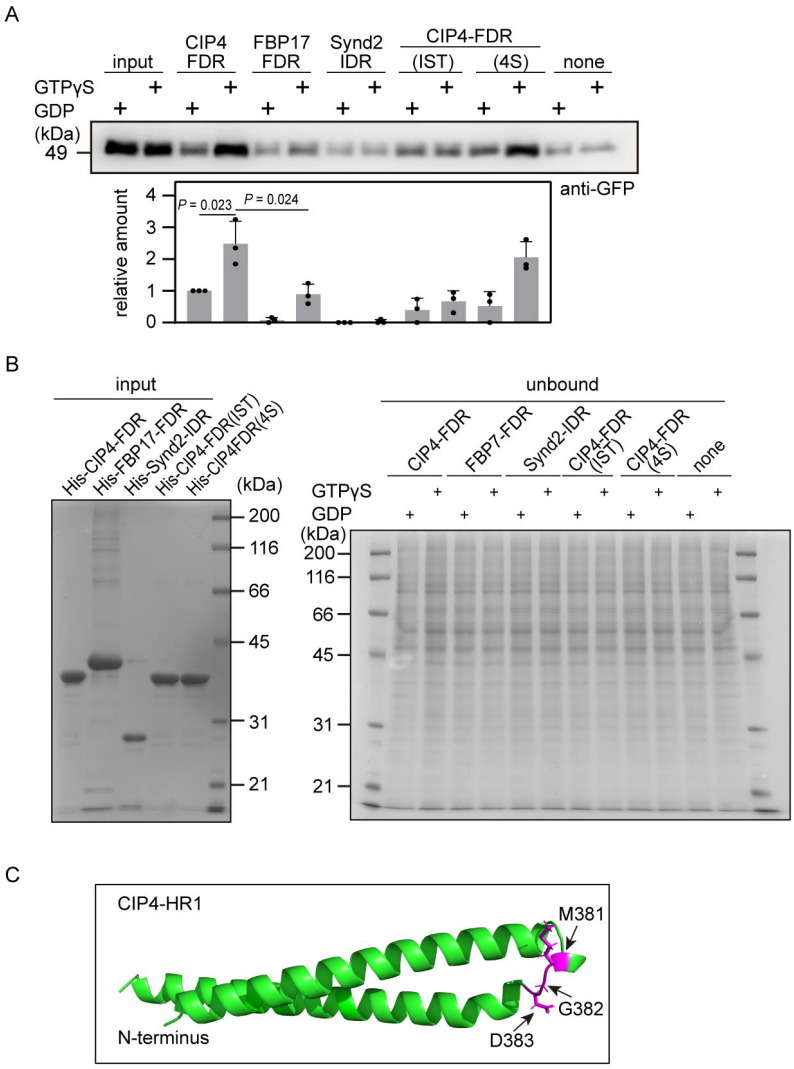

Figure 2-10. CIP4 interacts with activated Cdc42 via FDR.

A, Pull-down assay between activated or inactivated Cdc42 and CIP4-FDR, FBP17-FDR, Synd2-IDR, CIP4-FDR(IST), or CIP4-FDR(4S). Cdc42 expressed in the cell lysate was incubated with either GDP or GTP-γS and mixed with hexa-histidine-tagged recombinant proteins. Subsequently, the eluted fraction was analyzed using western blotting, and the results are summarized in the bottom panel. The data are presented as the mean ± standard deviation from three independent experiments. All data points are shown. *P* values were calculated using the two-tailed Student's *t*-test, $\alpha = 0.05$.

B, SDS-PAGE analysis of the input and the unbound fraction of the pull-down assay presented in (A).

C, A three-dimensional structure of CIP4-HR1 predicted by AlphaFold2. Three mutated residues in CIP4(IST) (M381, G382, D383) are indicated in magenta.

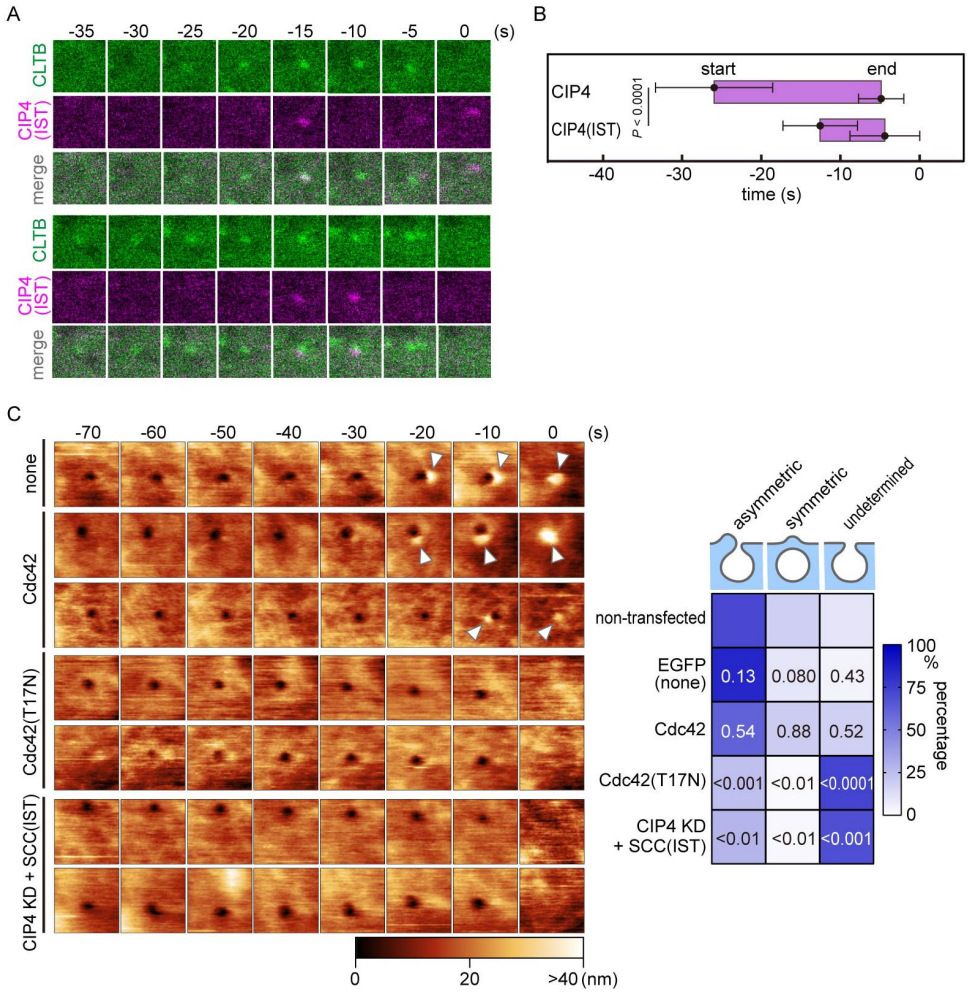

Figure 2-11. Cdc42 recruits CIP4 to the CCP.

A, Time-lapse fluorescence images of Cos7 cells co-expressing EGFP-fused CLTB and mCherry-fused CIP4(IST) mutants. The image size is 1.0 × 1.0 μm^2. Time 0 was defined as the time point when the clathrin signal of the CCP disappeared.

B, Summary of the CIP4 and CIP4(IST) assembly at the CCP. The time when the fluorescence signal appeared and disappeared at the CCP area was defined as 'start' and 'end', respectively, and plotted (N = 20, for each condition). *P* values were calculated using the two-tailed Student's *t*-test, α = 0.05. Error bars represent the standard deviation.

C, Time-lapse HS-AFM images obtained from Cos7 cells expressing EGFP (none) or EGFP-fused Cdc42 (WT or T17N mutant) and from Cos7 cells depleted with CIP4 followed by the expression of EGFP-fused SCC(IST). The frame rate is 0.1 frame/s, and the image size is 1.0 × 1.0 μm^2. Time 0 was defined as the time point when the clathrin signal of the CCP disappeared. The position of the membrane bulge is indicated with arrowheads, and the height information of the AFM image is provided using a colour bar. The frequency of three closing patterns was measured and is summarised in the right panel (N = 4 for each condition).

2.4 Discussion

In this chapter, I described that the asymmetric closing requires CIP4 and CIP4-mediated actin signalling. Interestingly, treatments that reduced the frequency of asymmetric closing also inhibited the symmetric closing, such as the knockdown of CIP4 or N-WASP and the addition of CK666 (Figure 2-2A and 2-9A). Moreover, the expression of CIP4 under the knockdown background rescued the formation of membrane bulge (asymmetric and symmetric) (Figure 2-5D). These observations demonstrate that CIP4-induced actin polymerization is necessary for both the asymmetric and symmetric bulge. However, expressing the chimeric molecules, such as SCC and SC, rescued only the asymmetric closing but not the symmetric one (Figure 2-9A), suggesting that the F-BAR region of CIP4 is necessary for the symmetric bulge. One possible scenario is that the self-assembly of the F-BAR domain is not enough to support the asymmetric distribution of CIP4; however, when the local concentration of CIP4 is higher than a certain threshold, the F-BAR domain of CIP4 could lead to a near-symmetric distribution of CIP4 around the CCP, leading to the formation of the symmetric bulge.

The Deeply-invaginated CCV is connected to the plasma membrane by a long and thin tabulated membrane. The dominant asymmetric closing of CCP suggests that the constriction or scission of the membrane tubules is likely to be non-axisymmetric. Mathematical simulation of the budding process revealed that a significant amount of energy is required to symmetrically constrict a narrow elastic tubule owning to radical pressure [69]. On the contrary, reducing the symmetry of the membrane tubule, like crushing a soda bottle remarkably decreased the energy barrier (roughly one order of magnitude) for membrane pinching, which is more favourable to live-cell surface [69]. In good agreement with these findings, I observed that the asymmetric closing is much faster than the symmetric one (Figure 2-2B), suggesting that asymmetric constriction is more efficient in the budding of CCVs. However, when the membrane bulge is absent (undetermined closing), the closing rate

is comparable to that of the asymmetric one (Figure 2-2B). Previous observation revealed that this closing motion was usually accompanied by the frequent "re-open" of the CCP [27]. One of the explanations is that the membrane bulge promotes the fusion of the plasma membrane from one side of the CCP to the other side and that the CCV failed to completely detach from the membrane when the bulge was not formed, suggesting that the asymmetric bugle is necessary for the complete closing of the CCP.

The burst accumulation of actin filaments induced the asymmetric bulge formation (Figure 2-2A and 2-3C), suggesting that the distribution of actin around the CCP is also asymmetric. Electron microscopy and recent super-resolution microscopy have directly observed and analysed this [51, 70]. Given the fact that dynamin is not indispensable for the constriction and scission processes and that actin was believed to be the significant force generator for vesicle budding during clathrin-independent endocytosis [32, 71], it would be reasonable to assume that, when the actin abundancy is high, actin-mediated pit-closing may compensate for the dynamin-driven pit-closing. Indeed, it has been shown that the asymmetric actin preferred to polymerize around the CCV stalled at the plasma membrane owing to great membrane tension and pushed the vesicle into the cytosol, similar to a bottle opener pulling off a bottle cap [70].

2.5 Materials and Methods

Plasmids

Fragments of full-length (FL) CLTB (amino acids (a.a.) 1–229) were amplified using PCR and subcloned into pmCherry-N1 or pEGFP-N1 vectors for mammalian expression. Fragments of the full-length CIP4 (a.a. 1–547), FL-FBP17 (a.a. 1–617), and FL-Synd2 (a.a. 1–486) were amplified using PCR and subcloned into pmCherry-C1 or pEGFP-C1 vectors. Fragments of FL CIP4, CIP4-FDR (a.a. 258–489), FBP17-FDR (a.a. 258–552), and Synd2-

IDR (a.a. 276–428), were amplified using PCR and subcloned into pET28a (+) vectors for expression in *Escherichia coli*.

Fragments of the CIP4-F-BAR (a.a. 1–257), CIP4-FDR (a.a. 258–489), and CIP4(ΔSH3) (a.a. 1–489) were amplified using PCR and subcloned into pmCherry-C1 vectors for mammalian expression. The SCC chimaera fragment was obtained by amplifying and ligating the nucleotide sequence corresponding to Synd2 (a.a. 1–275) and CIP4 (a.a. 258–547) using PCR and was subcloned into pmCherry-C1 and pEGFP-C1 vectors. The SC chimaera fragment was obtained by amplifying the S-C region from the SCC fragment using PCR and was subcloned into pmCherry-C1 and pEGFP-C1 vectors.

Single and multiple amino acid mutation was introduced using PrimerSTAR® Max DNA Polymerase (Takara Bio Inc., Shiga, Japan) according to manufacturer's instructions. The W524K mutation was generated by substituting the amino acids of W524 with K. To generate the IST mutation, amino acids of M381, G382, and D383 were replaced with I, S, and T, respectively.

Fragments of CIP4-HR1 (a.a. 339–425), CIP4-SH3 (a.a. 490–547), and N-WASP-GBD (a.a. 202–259) were amplified using PCR and subcloned into pET28a (+) or pGEX-6P-1 vectors. Fragments of FL N-WASP (a.a. 1–506) or FL Cdc42 (a.a. 1–191) were amplified using PCR and subcloned into pmCherry-C1 and pEGFP-C1 vectors, respectively. pcDNA3-EGFP-Cdc42(T17N) was purchased from Addgene (plasmid # 12600) [72].

Cell culture, transfection, and pharmacological treatment

Cos7 cells, fibroblasts derived from monkey kidneys, were obtained from the Cell Engineering Division at RIKEN BioResource Center (RBC0539; Ibaraki, Japan) and were cultured in high-glucose Dulbecco's modified Eagle's medium (DMEM) supplemented with 10% fetal bovine serum (FBS) at 37 ℃ with 5% CO_2. Polyethyleneimine (M.W. 40,000,

Polyscience, Niles, IL, USA) was used to transfect Cos7 cells according to manufacturer's instructions.

For HS-AFM observations, Cos7 cells were seeded on slide glasses (Matsunami Glass Ind., Ltd., Osaka, Japan) coated with a 0.01% poly-L-lysine solution (Sigma-Aldrich, St. Louis, MO, USA) and incubated at 37 ℃ for 1 hour. For correlative imaging of HS-AFM and confocal microscopy, cells were seeded on 0.15 CG pierced slide glass (ToA Optical Technologies, Inc., Tokyo, Japan) instead. HS-AFM observations were conducted 24 h after cell seeding.

To inhibit actin polymerization and examine its effects on CCP closing, CK666 (Abcam, Cambridge, United Kingdom) was added to the DMEM to a final concentration of 100 μM 30 minutes before the HS-AFM observation to allow sufficient time for the compound to take effect.

Expression and purification of recombinant proteins

In this Chapter, the following recombinant proteins were used: hexa-histidine-tagged CIP4, CIP4-HR1 and glutathione S-transferase (GST)-tagged CIP4-SH3, CIP4-SH3(W524K), and N-WASP-GBD. Recombinant protein-encoding vectors were transfected into competent BL21-CondonPlus (DE3)-RIL cells (Agilent Technologies, Inc., Santa Clara, CA, USA) by heat shock at 37 °C for 30 seconds. To induce expression of the recombinant protein, 0.5 mM isopropylthio-β-D-galactoside was added, and cells were incubated at 16 °C for 16 hours. Bacterial cells expressing recombinant proteins tagged with hexa-histidine were harvested and suspended in phosphate-buffered saline (PBS; pH 7.4) containing lysozyme (0.2 mg/mL), DNaseI (20 μg/mL), MgCl2 (1 mM), and phenylmethanesulfonylfluoride (1 mM). Freeze-thaw cycles were repeated three times, followed by sonication to homogenize the cells. Centrifugation at 13,000 g, 4 °C for 15 minutes was then applied to remove insoluble cell

debris. The clarified lysate was combined with nickel-nitrilotriacetic acid (Ni-NTA)-agarose beads (QIAGEN) or glutathione (GSH) Sepharose 4B beads (Cytiva) and incubated at 4 °C for 1 hour with rotation to bind the tagged proteins. Elution buffer A (pH 7.4; 100 mM NaCl, 50 mM HEPES, 0.2 mM DTT, and 400 mM Imidazole) were used to elute the hexa-histidine-tagged proteins. Elution buffer B (pH 7.4; 100 mM NaCl, 50 mM HEPES, 0.2 mM DTT, and 200 mM GSH) were used to elute the GST-tagged proteins. Eluted proteins were dialysis against dialysis buffer containing 200 mM NaCl and 50 mM HEPES (pH 7.4) at 4 °C for 6 hours. The proteins were concentrated using AmiconUltra (M.W. 3,000 Da; Sigma-Aldrich) and stored at -80 °C until further use.

Pull-down assay

Approximately 5 μg of the recombinant proteins were immobilized on approximately 20 μL of Ni-NTA agarose or GSH Sepharose 4B beads. HEK293T cells were used to express EGFP-fused Cdc42 and EGFP-fused N-WASP. The cell pellet was suspended in ice-cold PBS containing Protease Inhibitor Cocktail (0.5%, Nacalai Tesque, Inc.) and Triton-X-100 (0.25%) for 10 minutes. EGFP-Cdc42 expressed in cell lysate was incubated with GTPγ-S to activate it *in vitro* or with GDP to keep it inactive as described previously [73]. The EGFP-Cdc42 in cell lysate was then combined with the purified recombinant protein and Ni-NTA or GSH beads, followed by incubation at 4 °C for 25 minutes. The bounded protein was eluted with 400 mM imidazole or 100 mM GSH in Elution Buffer (pH 7.4; 100 mM NaCl, 50 mM HEPES, 0.2 mM DTT). Immunoblotting and SDS-PAGE were used to analyze ~20% of the bound fraction and ~10% of the unbound fraction, respectively.

RNA interference

siRNA against CIP4 (ID: s17814), FBP17 (ID: s22916), or Synd2 (ID: s22216) were

purchased from Ambion Inc. (Austin, TX, USA). siRNA against N-WASP (siGENOME SMART pool) was purchased from Dharmacon Inc. (Lafayette, CO, USA). siRNA targeting the 3′UTR sequence of CIP4 was customised at Thermo Fisher Scientific. HiPerfect reagent (QIAGEN, Hilden, Germany) was used to transfect Cos7 cells with siRNA according to the manufacturer's protocol. After 48 hours of transfection, the cells were trypsinized and either seeded onto slide glasses or directly harvested for analysis using sodium dodecyl sulfate-polyacrylamide gel electrophoresis (SDS-PAGE) followed by immunoblotting.

To perform rescue experiments, Cos7 cells were transfected with siRNA against CIP4 48 h before the HS-AFM observation followed by the transfection of vectors encoding EGFP-tagged CIP4 24 h before the observation.

Immunoblotting

Cos7 cell lysates with N-WASP knockdown were loaded onto a 12% SDS-PAGE gel, and the proteins were then transferred to a polyvinylidene difluoride membrane. The membrane was blocked with 5% skimmed milk in tris-buffered saline (5 mM Tris, 13.8 mM NaCl, 0.27 mM KCl, pH 7.4) containing 0.1% Tween (Nacalai Tesque, Inc., Kyoto, Japan) and incubated with a primary antibody for 1 hour. The primary antibodies used were as follows: rabbit anti-N-WASP (1:1000; Cell Signaling Technology, Danvers, MA, USA), rabbit anti-CIP4 (1:1000; Bethyl Laboratories Inc., Montgomery, TX, USA), rabbit anti-FNBP1 (1:1000; Novus Biologicals LLC), rabbit anti-Pacsin2 (1:1000; Novus Biologicals LLC, Centennial, CO, USA), rabbit anti-GFP (1:1000; Medical & Biological Laboratories Co., Ltd., Nagano, Japan), and mouse anti-β-actin (1:1000; Sigma-Aldrich). Following this, the blot was subjected to incubation with the respective secondary antibodies: goat anti-rabbit IgG (H+L) antibody (1:5000; Thermo Fisher Scientific, Waltham, MA, USA) or goat anti-mouse IgG (H+L) antibody (1:5000; Cytiva, Marlborough, MA, USA) at 27 °C for 1 hour. A LAS-3000 Imager (Fujifilm, Tokyo, Japan) and Chemi-Lumi One Super Kit (Nacalai Tesque,

Inc.) were used to visualize the immunoreactive bands according to manufacture's instructions.

HS-AFM imaging

The AFM imaging was performed using a tip-scan type HS-AFM system (BIXAM^{TM}; Olympus Corporation, Tokyo, Japan) combined with a confocal microscope (FV1200, Olympus Corporation). The HS-AFM system employed tapping mode with phase feedback control and utilized an electron beam-deposited ultra-short cantilever (USC-F0.8-K0.1-T12-x66-10; Nonoworld Corporation, Neuchâtel, Switzerland) with a spring constant of 0.1 N m^{-1}. The free amplitude of the cantilever during HS-AFM imaging was set at ~90%. To perform a detailed analysis of the morphological characteristics of the undetermined closing pattern, images were acquired every 2 seconds. However, for more general observation of clathrin pits, images were acquired every 10 seconds, considering the trade-off between scanning speed and area. At this setting, the total scanning area was 6000 × 4500 nm^2, displayed in 320 pixels × 240 pixels images. All observations were conducted at a constant temperature of 28 ℃.

Time-lapse HS-AFM images were captured using the AFM Scanning System Software Version 1.6.0.12 (Olympus Corporation). The analysis of the diameter, duration, and height of the membrane bulge was performed using Gwyddion software (ver 2.55; http://gwyddion.net/) and GIMP software (ver 2.10.18; https://www.gimp.org/). To determine the height of the membrane bulge, the highest point of the plasma membrane within the CCP area was recorded and compared to the surrounding plasma membrane. The lowest position in the HS-AFM image was used as the reference point (labelled as '0'). The duration of the membrane bulge was calculated from the appearance to the disappearance of the bulge in HS-AFM. To measure the size of the pit aperture, the maximum diameter throughout the entire CME process was obtained by performing a cross-section and measuring the distance

between one side of the pit and the other. In cases where no detectable membrane bulge was observed (undetermined pattern), both the height and duration were assigned as '0 μm' and '0 s', respectively. The growth rate of the membrane bulge was determined by plotting the change in membrane height at the pit area against time, focusing on the ascending part of the height-time plot. Conversely, the closing rate of CCPs was obtained by examining the slope of the descending part of the diameter-time plot.

Correlative imaging of HS-AFM and CLSM

To achieve correlative imaging between HS-AFM and CLSM, proper alignment of AFM and fluorescence microscopy images is necessary, as previously described [27]. In summary, the cantilevers were securely positioned on a holder at an approximate tilted angle of 12 degrees relative to the x-y plane. This arrangement ensured that the tip of the cantilever and the sample stage formed an almost 90-degree angle, facilitating precise identification of the cantilever position under the optical microscope. Additionally, the cantilever exhibited autofluorescence, enabling its visualization via confocal microscopy. This autofluorescent spot served as a reference point for aligning the cantilever in both HS-AFM and CLSM imaging. The coordinates of the fluorescence spot were defined as (0, 0). Both HS-AFM and CLSM were conducted at a frame rate of 0.1 frame/s once the imaging commenced.

Live-cell fluorescence microscopy

Live-cell imaging was conducted using a confocal laser-scanning microscope (FV3000, Olympus Corporation) equipped with a stage incubator (TOKAI HIT Corporation, Shizuoka, Japan). The optimized operation of the microscope allows for a lateral spatial resolution of ~200 nm. All imaging was performed under 37 °C with a CO_2 concentration of 5.0%. Cos7 cells cultured in a 30-mm glass-bottom dish with ~40% of confluence were

transfected with mammalian expression plasmids 24 hours before observation. Fluorescence images were captured at 5-second intervals and subsequently analyzed using ImageJ (ver 1.52a; https://imagej.nih.gov) and the GIMP software (ver 2.10.18; https://www.gimp.org/).

Super-resolution SIM live-cell imaging

Super-resolution SIM was conducted using the Elyra 7 system with Lattice SIM^2 (Zeiss, Oberkochen, Germany). The optimal lateral spatial resolution is ~60 nm. For live-cell imaging, Cos7 cells transfected with vectors encoding EGFP-fused CLTB and mCherry-fused CIP4 were seeded on a 30-mm glass-bottom dish at a density of 40% 24 hours before imaging. The culture medium in the dish was replaced with phenol red-free DMEM (Sigma-Aldrich) 30 minutes before imaging. Images were captured every 0.5 seconds and processed using the Zeiss Enz 3.6 blue edition software (Zeiss). Subsequent analysis of the images was performed using ImageJ (ver 1.52a; https://imagej.nih.gov).

Disordered regions prediction

The prediction of disordered regions in CIP4, FBP17, and Synd2 was performed using IUPred3 (https://iupred3.elte.hu/) [74]. The amino acids sequence of CIP4, FBP17, and Synd2 is shown in Figure 2-7B.

Multiple sequence alignment

T-Coffee test (https://www.ebi.ac.uk/Tools/msa/tcoffee/) [75] was used to perform multiple sequence alignment. EMBOSS Needle (https://www.ebi.ac.uk/Tools/psa/emboss_needle/) was used to calculate the sequence similarity. The amino acid sequence of CIP4, FBP17, and Synd2 is shown in Figure 2-7B.

Three-dimensional protein structure predictions

The three-dimensional structure of the CIP4-HR1 domain was predicted by ColabFold (v.1.5.2: AlphaFold2 using MMseqs2) (https://colab.research.google.com/github/sokrypton/ColabFold/blob/main/AlphaFold2.ipynb) [76, 77]. The amino acids sequence shown in Figure 2-7B was used for the prediction.

Chapter 3. Self-assembly of CIP4 drives 'asymmetric' actin machinery

3.1 Introduction

Aside from CIP4, AP2, Eps15, FCHO, intersectin, epsin, and other endocytic proteins usually possess distinct spatial localization instead of evenly distributed around the clathrin pit as previously demonstrated by dual colour total internal reflection fluorescence microscopy and correlative super-resolution light and transmission electron microscopy [65, 78]. Although the biological significance of the asymmetric distribution is not fully understood, it is reasonable to assume that the specific localization of endocytic proteins is closely associated with their functions during CME progression.

Actin is not indispensable but still contributes to multiple steps in the progression of CME in mammalian cells, including membrane bending, constriction, scission, and vesicle translocation [79, 80]. Electron microscopy and topography revealed that the morphology of the actin network around clathrin pits are variable, including small patches that are close to slightly invaginated CCPs, collar-shaped dense network surrounding deeply invaginated CCVs, and comet tail-like structure associated with CCVs that utterly detached from the membrane indicating that actin is a multi-functional unit during CME [51].

Recent live-cell imaging of mammalian endocytosis using superresolution techniques revealed that actin and actin nucleators, including Arp2/3 complex and neuronal wiskott-aldrich syndrome protein (N-WASP) asymmetrically assembled around the CCP, especially around those that were stalled at the plasma membrane [70], suggesting that the asymmetric actin machinery may function as an essential force to drive the invagination of internalization of the CCV. Actin was recruited to the CCP in mammalian cells and started accumulating before the complete pit closure [27]. Pharmacological interference of the actin turnover in Swiss 3T3 (mouse fibroblasts) or A431 (epidermoid carcinoma) cells significantly inhibited the vesicle formation and the internalization of transferrin receptors [79, 81]. Although detailed

mechanisms about how actin contributes to membrane bending have not been thoroughly dissected, it has been demonstrated that similar to the role of the actin cytoskeleton driving membrane deformation in yeast, actin polymerization is a vital force generator aside from clathrin in mammalian cells to counteract membrane tension and promote CCP invagination [82]. An interesting theory claimed that the generation of pushing force to drive vesicle invagination requires the dynamics of actin assembly and disassembly mediated by nucleation factors, including actin-related protein 2/3 (Arp2/3) complex and depolymerization factors such as cofilin resulting in the formation of arrays of short-branched actin filaments, machinery usually to explain how actin polymerization push forward the leading edge in a migrating cell [5, 83].

Moreover, actin interplays with and assists the function of other endocytic proteins, such as dynamin and F-BAR domain proteins. FBP17 is known to induce the long membrane tubules at the neck of the CCV via the end-to-end joint of the F-BAR domain [59, 84]. Enhanced actin polymerization by overexpression of N-WASP notably inhibited the formation of membrane tubules, while the treatment of latrunculin B, an inhibitor of actin polymerization, promoted the elongation of the tabulated membrane, indicating that actin polymerization might affect membrane tabulation [84]. In good agreement with this, it has been reported that membrane tabulation requires the intact actin cytoskeleton at the site of CME, and further investigation suggested that dynamin 'cut' the actin-mediated tabulation based on the observation that the CCV was stalled at the sites of endocytosis together with robust actin accumulation upon the knockout of dynamin [48]. More recent studies revealed that actin assembly promote the assembly of dynamin, and in turn, each dynamin helix can align 12–16 actin filaments into bundles to accelerate actin polymerization [85, 86].

Based on these findings, illustrating the molecular mechanisms of the asymmetric actin polymerization and demonstrating the functional crosstalk between actin and other endocytic proteins would significantly enhance our understanding of the machinery of the

CCP closing process during CME.

3.2 Objective

Assuming that the assembly of CIP4 is merely dependent on the F-BAR domain, there should be no structural basis for the asymmetric distribution around the CCP, as I observed in Figure 2-6C. Indeed, I have shown that the dynamic of CIP4 at CCP is affected mainly by its FDR. In this chapter, I aim to explain the driving force for the asymmetric CIP4 assembly and how it contributes to the actin polymerization around the CCP.

3.3 Results

3.3.1 CIP4 asymmetrically self-assembles via FDR

In Chapter 2, I demonstrated that CIP4 assembled before the complete CCP closing, interacted with Cdc42 and N-WASP, and induced the formation of membrane bulge. Nevertheless, it fails to explain the generation of 'asymmetricity.' One potential mechanism could involve the cooperative assembly of CIP4. Structural predictions based on the amino acid sequence suggest that the HR1 domain of CIP4 consists of two antiparallel α-helices (Figure 3-1A). To investigate the secondary structure of CIP4-HR1, I conducted circular dichroism (CD) measurements on recombinant HR1, which exhibited a pronounced propensity for α-helix, closely resembling the reference curve (Figure 3-1B). This led us to speculate that HR1 may undergo multimerization, with the association occurring cooperatively. To test this hypothesis, I subjected purified HR1 to gel-filtration chromatography to estimate its molecular size. The results revealed that HR1 primarily exists as a dimer under physiological conditions, and no higher-order multimers were detected (Figure 3-1C and D). Similarly, when purified HR1 was treated with bis(sulfosuccinimidyl)suberate (BS^3) crosslinkers and analyzed using silver staining, the

addition of crosslinkers induced an additional band corresponding to the HR1 dimer (Figure 3-1E). These findings demonstrate that HR1 multimerization is not the predominant driving force of asymmetricity.

An alternative possibility involves the phase transition of FDR through electrostatic interactions among disordered regions. Disordered regions at the amino and carboxyl sides of CIP4-HR1 and FBP17-HR1 are positively and negatively charged, respectively (Figure 3-2A). Conversely, the segregation of charges in Synd2 IDR is less pronounced (Figure 3-2A). It has been reported that a polymer with charge segregation, referred to as a block polyampholyte, exhibits more robust liquid-liquid phase separation (LLPS) compared to a chain with randomly distributed charges (random polyampholyte) [87, 88]. Furthermore, the arrangement of charge blocks plays a critical role in determining the properties of LLPS [89]. These distinctive characteristics strongly suggest that FDR undergoes self-assembly and LLPS via charge-block interactions. I conducted an in vitro droplet assay using purified proteins with polyethylene glycol as a crowder to investigate this possibility. CIP4-FDR instead of Synd2-IDR formed protein droplets (Figure 3-2B). Quantitative analysis of protein droplets based on turbidity assay demonstrated that the saturation concentration (C_{sat}) of CIP4-FDR resembled that of FBP17-FDR but was significantly lower than that of Synd2-IDR, indicating a higher propensity for LLPS in CIP4-FDR and FBP17-FDR compared to Synd2-IDR (Figure 3-2B and C). Fluorescence recovery after photobleaching (FRAP) analysis revealed that the protein droplets were liquid-like (Figure 3-2D). Deletion of either IDR1 or IDR2 from CIP4-FDR markedly attenuated LLPS (Figure 3-2C and E), providing compelling evidence for the indispensable role of charge block interactions in the self-assembly of FDR.

However, neither the deletion of IDR1 nor IDR2 eliminated the LLPS of CIP4-FDR, suggesting that HR1 also contributes to this phenomenon. A partial but significant reduction in LLPS propensity was observed upon HR1 deletion (ΔHR1) (Figure 3-2C and E).

Moreover, I found the disruption of HR1 dimer formation by substituting four hydrophobic residues (L347, L401, Y408, and W411) with serine (4S) effectively disrupted HR1 dimerization (Figure 3-1A and C) while maintaining the interaction with Cdc42 (Figure 2-10A). As anticipated, CIP4-FDR(4S) mutants have lower LLPS propensity than that of the WT (Figure 3-2C and E), suggesting that HR1 dimerization may promote the LLPS of FDR (Figure 3-2F).

To examine the effect of FDR-driven LLPS on CIP4 assembly, I assessed the assembly rate of CIP4 at CCP. Deletion of the SH3 domain (CIP4(ΔSH3)) did not affect the assembly rate at the CCP (Figure 3-3A). However, further deletion of IDR2 (ΔIDR2/SH3), which reduces the LLPS propensity of CIP4-FDR as I described, resulted in a significant reduction (~70%) in the assembly rate (Figure 3-3A). Likewise, the 4S mutation in FL CIP4 almost wholly abolished the assembly, exhibiting a more severe effect than IDR2 deletion (Figure 3-3B). Consistent with this finding, the SCC chimeric construct carrying the 4S mutation failed to rescue the asymmetric bulge (Figure 3-3C). These observations provide strong evidence for the critical role of FDR-dependent LLPS in CIP4 assembly.

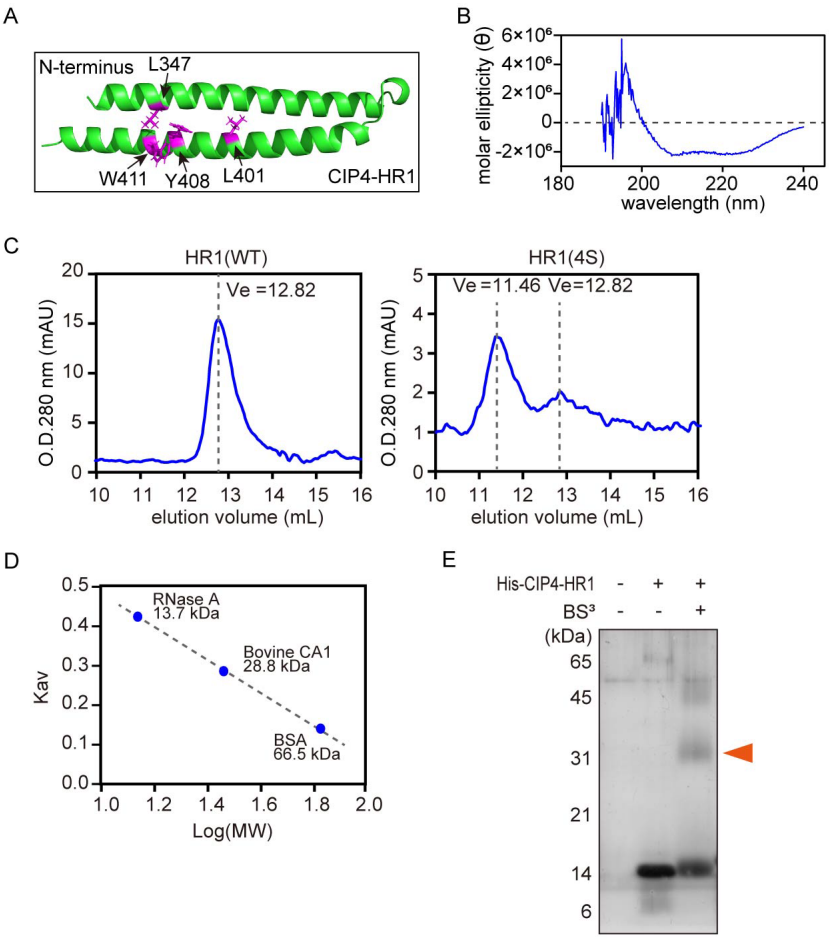

Figure 3-1. CIP4-HR1 dimerizes in physiological conditions.

A, The AlphaFold2-predicted three-dimensional structure of the CIP4-HR1 with mutated residues in CIP4-HR1(4S) highlighted in magenta.

B, CD spectrum of *in vitro* purified CIP4-HR1.

C, Gel-filtration chromatography of purified CIP4-HR1(WT) and CIP4-HR1(4S). The absorbance at 280 nm (mAU) is plotted against the elution volume (mL), with the peak position (V_e) indicated by a dotted line.

D, A size calibration of the gel-filtration chromatography shown in (C). RNase A (13.7 kDa), bovine carbonic anhydrase 1 (BCA1, 28.8 kDa), and bovine serum albumin (BSA, 66.5 kDa) were analysed. The partition coefficient (K_{av}) obtained from the chromatogram is plotted against the molecular weight.

E, Crosslinking assay of purified CIP4-HR1. Non-treated and bis(sulfosuccinimidyl)suberate (BS^3)-treated CIP4-HR1(WT) were subjected to SDS-PAGE and subsequent silver staining. The speculated HR1 dimer band is indicated with an arrowhead.

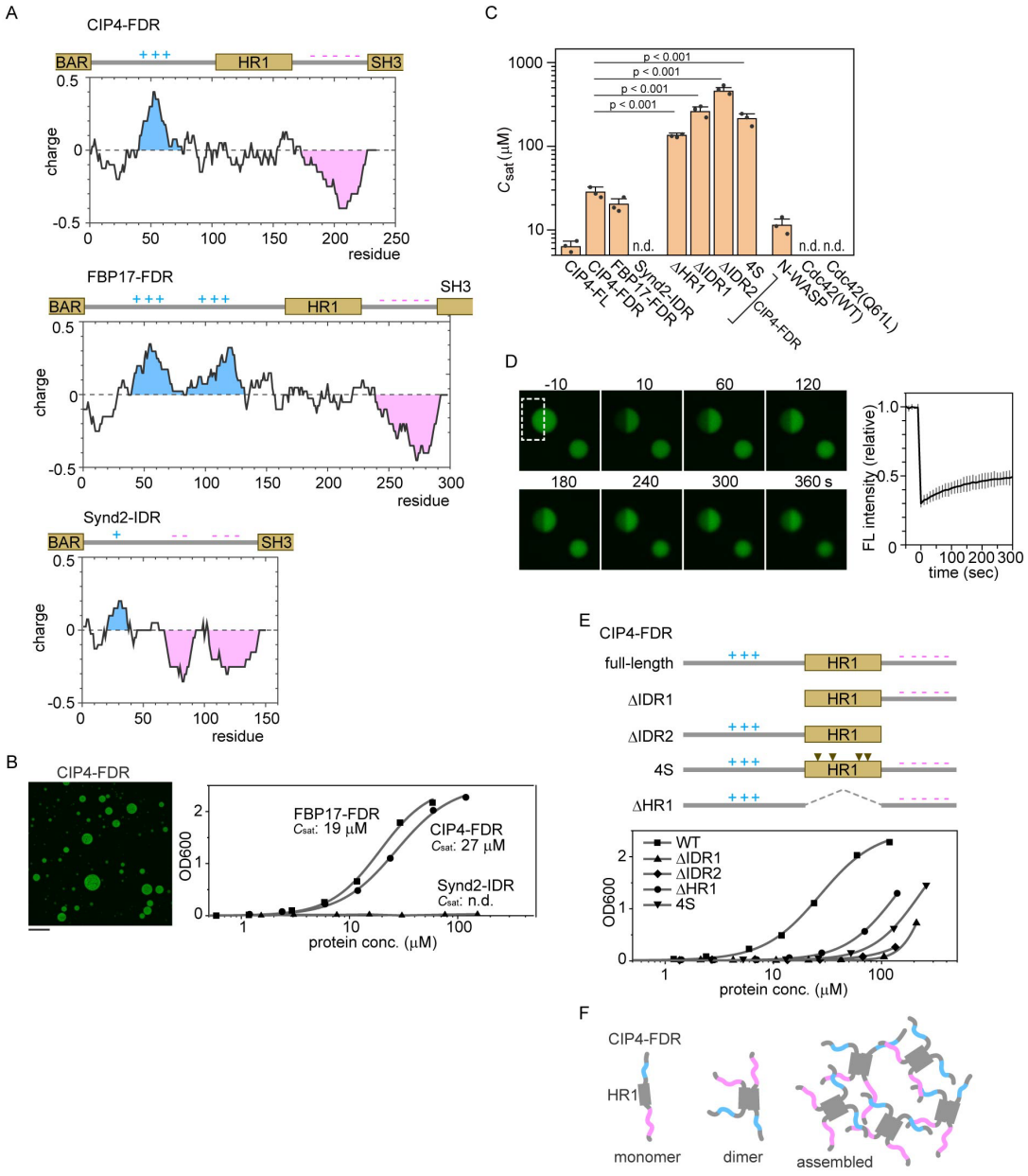

Figure 3-2. CIP4-FDR undergoes LLPS *in vitro*.

A, Electrostatic charge plots of CIP4-FDR, FBP17-FDR, and Synd2-IDR. In CIP4 and FBP17, the FDR has a net positive (marked in blue) and a net negative (marked in red) IDRs.

B, *In vitro* phase separation of CIP4-FDR and turbidity assay of CIP4-FDR, FBP17-FDR and Synd2-IDR. The turbidity was measured based on optical density at 600 nm and plotted against the protein concentration. The C_{sat} is indicated. A representative microscopic image of the CIP4-FDR droplet, pre-labelled with ATTO488, is provided. Scale bar: 50 μm.

C, The summary of the C_{sat} obtained from the turbidity assay. *P* values were calculated using

the two-tailed Student's *t*-test, $\alpha = 0.05$. Error bars represent the standard deviation from three independent experiments. All data points are shown. n.d. not determined.

D, FRAP analysis of a protein droplet formed by CIP4-FDR. The region indicated by a dotted square was bleached via laser radiation. The average fluorescence intensity of the bleached region was quantified and plotted against time. The intensity of the pre-bleached signal is set as 1. Data are presented as mean ± standard deviation from three independent measurements. Images were taken every 10 s.

E, (top) A schematic illustration of CIP4-FDR and its deletion mutants. (bottom) The turbidity assay was performed and analysed with the same procedures described in (B).

F, A schematic illustration of the LLPS of CIP4-FDR. The condensation is driven by charge block interaction and promoted by HR1 dimerization.

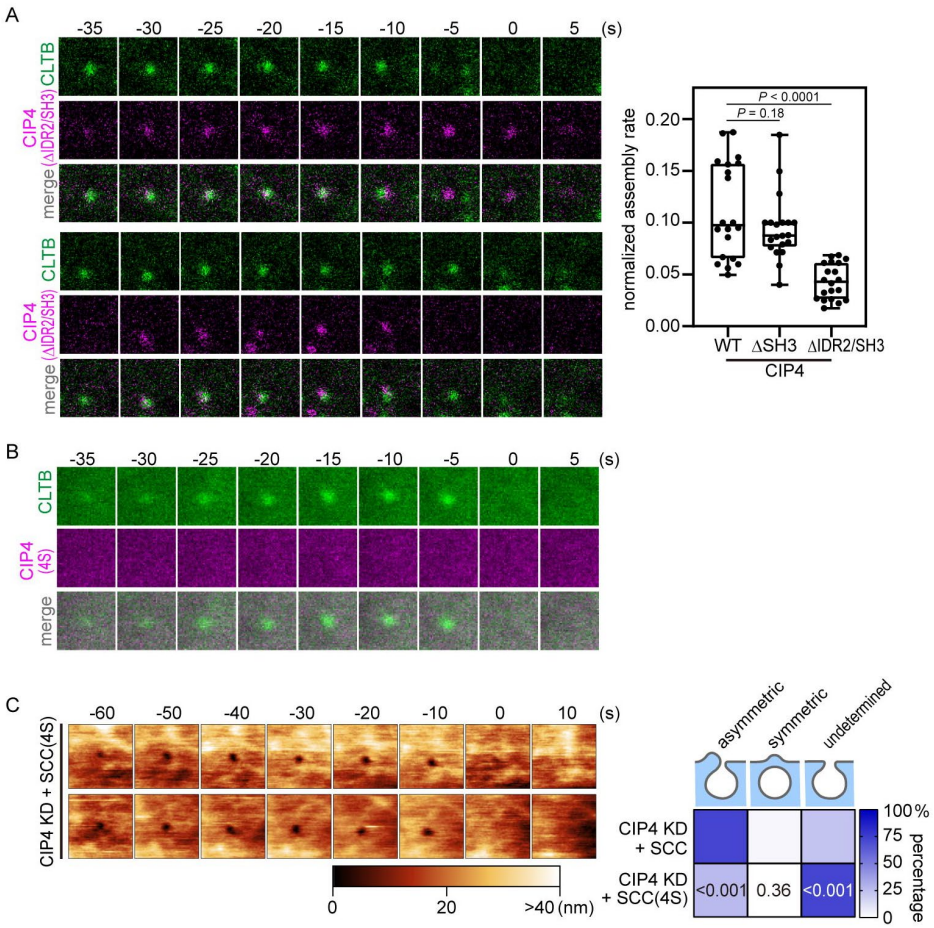

Figure 3-3. Phase separation of CIP4-FDR promotes the assembly of CIP4.

A, (Left) Time-lapse fluorescence images of Cos7 cells co-expressing EGFP-fused CLTB and mCherry-fused CIP4(ΔIDR2/SH3). Time 0 was defined as the time point when the clathrin signal of the CCP disappeared. Images were taken every 5 s. Image size: 1.0 × 1.0 μm^2. (Right) The assembly rate of CIP4, CIP4(ΔSH3), and CIP4(ΔIDR2/SH3) at the CCP. The box plot displays the median, lower quartile, and upper quartile values, and the range of data is represented by the upper and lower whisker, N = 20 for each condition. *P* values were calculated using the two-tailed Student's *t*-test, α = 0.05.

B, Time-lapse fluorescence images of Cos7 cells co-expressing EGFP-fused CLTB and mCherry-fused CIP4(4S). Time 0 was defined as the time point when the clathrin signal of the CCP disappeared. Images were taken every 5 s. Image size: 1.0 × 1.0 μm^2.

C, Time-lapse HS-AFM images obtained from Cos7 cells subjected to CIP4 KD followed by the transfection of plasmids encoding EGFP-fused SCC(4S). The frame rate is 0.1 frame/s, and the image size is 1.0 × 1.0 μm^2. Time 0 was defined as the time point when the clathrin

signal of the CCP disappeared. The position of the membrane bulge is indicated with arrowheads, and the height information of the AFM image is provided using a colour bar. The frequency of three different closing patterns was summarised in the right panel (N = 4 for each condition).

3.3.2 Self-assembly of CIP4 drives asymmetric actin machinery

The close association between CIP4 and actin-related proteins, including Cdc42 and N-WASP, has been demonstrated in Chapter 2, and I believe it would be necessary to investigate further the potential impact of these regulators or effectors on the LLPS propensity of CIP4.

I observed that Cdc42, including the WT and constitutively active form Q61L, did not undergo LLPS nor enhance the LLPS propensity of CIP4-FDR (Figure 3-2C and 3-4A). This suggests that the interaction between Cdc42 and CIP4 is not involved in the LLPS of CIP4. In contrast, N-WASP exhibited a strong propensity for LLPS, with a C_{sat} of ~10 μM (Figure 3-2C). Considering this observation, I explored whether N-WASP and CIP4 coexist within the same droplet or if they exclude each other. Remarkably, N-WASP and FL CIP4 or CIP4-FDR coexisted in the same droplet, indicating the robust propensity of both proteins for LLPS and their tendency to be present together in the same droplet (Figure 3-4B). The co-separation of CIP4 and N-WASP also provides a potential pathway to condense downstream actin regulators, such as the Arp2/3 complex.

Next, I explored the direct influence of the liquid phase formed by CIP4 on actin polymerization. Firstly, I induced LLPS of CIP4-FDR as previously described, followed by adding rhodamine-labelled G-actin (Figure 3-4C). Time-lapse observations of fluorescence microscopy revealed the rapid movement of actin into the droplet (Figure 3-4C). Quantitive analysis revealed that the concentration of actin within the droplet was ~100 times higher than that in the surrounding medium, indicating a significant accumulation of actin in the CIP4-FDR droplet.

Subsequently, I explored whether actin polymerization occurred within the droplet. By introducing ATP, Mg^{2+}, and a low concentration of G-actin (45 μg/mL) into the CIP4-FDR droplet solution, I induced actin polymerization specifically within the droplet (Figure 3-4C and D). Due to the low actin concentration in the diluted phase, actin polymerization was

rarely observed outside the droplet. However, fibrous actin structures were frequently detected within the droplet (Figure 3-4D). Notably, ATP depletion significantly reduced actin polymerization within the droplet (Figure 3-4D). Together, these findings demonstrated that CIP4 self-assembles via FDR, effectively concentrating G-actin, consequently enhancing actin polymerization.

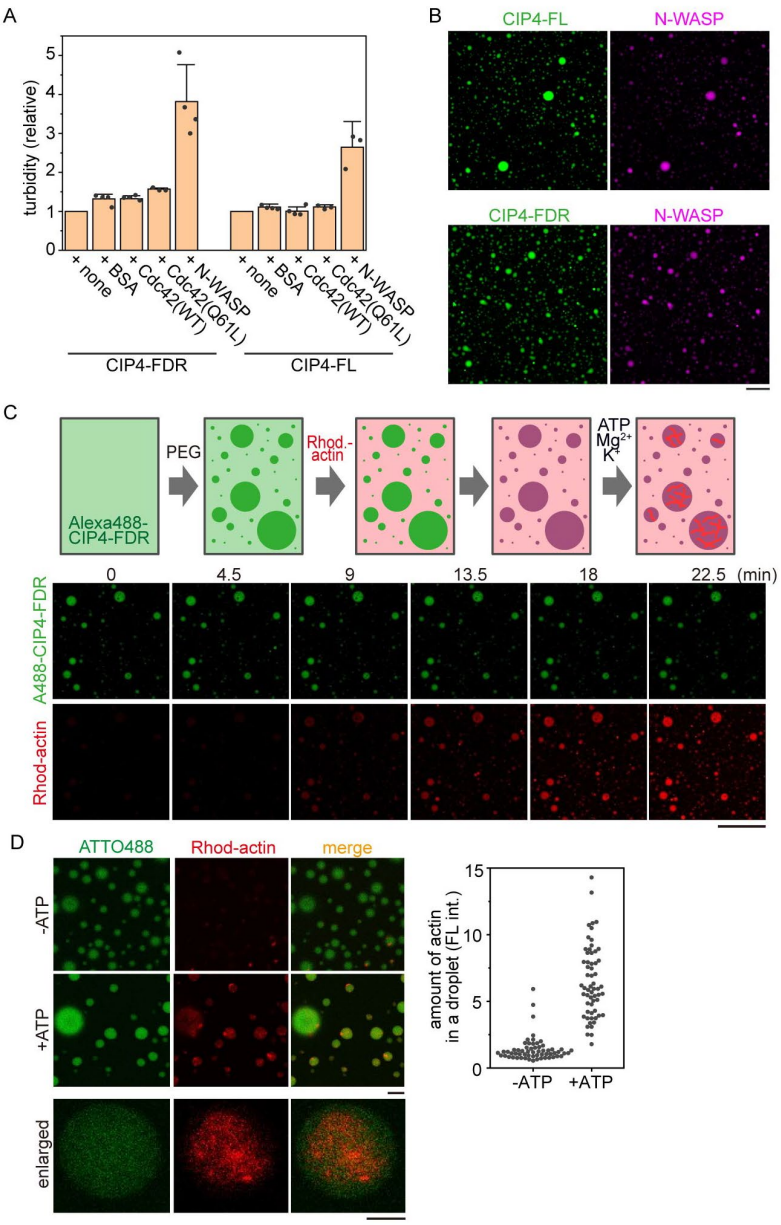

Figure 3-4. Phase separation of CIP4-FDR promotes actin polymerisation.

A, The LLPS propensity of CIP4 or CIP4-FDR is not affected by Cdc42. The relative turbidity of CIP4 (FDR and FL) in the presence or absence of Cdc42(WT), Cdc42(Q61L), N-WASP, and BSA was measured using turbidity assays and summarized. Data are presented as mean ± standard deviation from three independent experiments, and all data points are shown.

B, Co-separation of CIP4-FL or CIP4-FDR with N-WASP. The proteins were pre-labelled with ATTO488 (for CIP4-FL and CIP4-FDR) or ATTO610 (for N-WASP) for fluorescence imaging. Scale bar: 50 µm.

C, Actin polymerise within the CIP4-FDR droplet. (Top) Actin polymerization within the CIP4-FDR droplet is illustrated schematically. After the droplet formation of ATTO488-labelled CIP4-FDR, rhodamine-labelled G-actin was added, followed by ATP, Mg^{2+}, and K^{+}. (Bottom) Time-lapse fluorescence observation of the CIP4-FDR droplet (ATTO488-labelled) and G-actin (rhodamine-labelled). Scale bar: 100 μm.

D, (Left) Rhodamine-labelled and non-labelled G-actin (1:9) were incubated with or without ATP and Mg^{2+} and then with a pre-formed CIP4-FDR droplet. Enlarged images in the presence of ATP are shown. (Right) Quantification of the fluorescence intensity of F-actin observed in the droplet (N = 60 in each condition).

3.4 Discussion

In vitro, CIP4 exhibited robust self-assembly and underwent LLPS (Figure 3-2B and C). However, the estimated intracellular concentration of endogenous CIP4 (~20 nM, Figure 2-4C), was significantly lower than the C_{sat} (~6 μM, Figure 3-2C). These findings imply that, apart from the charge block-driven LLPS of FDR, additional mechanisms that facilitate the assembly of CIP4 near the CCP are necessary to initiate the phase separation. One explanation could be the stereospecific interactions mediated by the structured domains (F-BAR, HR1, and SH3). As I demonstrated in Chapter 2, CIP4 directly interact with membrane-bound and activated Cdc42 via the HR1 domain. At this stage, the local concentration of CIP4 might not reach the threshold required for initiating LLPS. However, when this interaction happens around the nucleation site of the CCP, the F-BAR domain of CIP4 senses the curved membrane structure and multimerizes on the membrane, which may lead to the increment of CIP4 concentration and allow the condensation of CIP4. Based on this assumption, it is worth noticing that FL CIP4 demonstrated a higher propensity for LLPS than FDR alone (Figure 3-2C), suggesting that the multimerization of the F-BAR domain may also promote the LLPS of CIP4.

Recent scientific investigations have shed light on a fascinating mechanism known as "membrane-assisted" LLPS, occurring in diverse intracellular membrane structures, including the plasma membrane [90, 91]. In this process, proteins anchored to or inserted into the membrane act as crucial "nucleation" sites for initiating LLPS. This membrane-centric, two-dimensional system exhibits a remarkable capability to accelerate LLPS compared to a dispersed protein solution, enabling LLPS to occur even when the overall protein concentration in the cytoplasm is below the conventional threshold. I propose that specific stereospecific interactions, such as Cdc42-HR1, F-BAR-F-BAR, and F-BAR-membrane, play a pivotal role in facilitating the nucleation of CIP4 near the CCP.

While the F-BAR domain can multimerize into a helical structure around tubulated

membranes *in vitro* [59], the mechanism does not explain the 'asymmetric' distribution around the CCP. Therefore, I speculate that LLPS plays a crucial role in the generation of 'asymmetricity', as the emergence of condensed phases occurs discontinuously when the local protein concentration exceeds a certain threshold. It is very likely that the combination of nucleation driven by the F-BAR domain and LLPS driven by FDR synergistically facilitates the rapid assembly of CIP4 at the CCP. These findings align with a previous study indicating that disordered domains enhance the binding of BAR domains to the curved membrane [92], further supporting the role of LLPS in CIP4 assembly.

3.5 Materials and Methods

Plasmids

Vectors encoding hexa-histidine-tagged CIP4-FDR, FBP17-FDR, Synd2-IDR, and CIP4-HR1 were constructed as described in Chapter 2. Fragments of FL Cdc42 (a.a. 1–191), N-WASP (a.a. 1–509), CIP4-FDR-ΔIDR1 (a.a. 339–489) and CIP4-FDR-ΔIDR2 (a.a. 258–425) were amplified using PCR and subcloned into pET28a (+) vectors for expression in *Escherichia coli*. Fragments of CIP4(ΔIDR2/SH3) (a.a. 1–425) were amplified using PCR and subcloned into pmCherry-C1 vectors for mammalian expression. The 4S mutation was generated by substituting the amino acids of L347, L401, Y408, and W411 with S using PrimerSTAR® Max DNA Polymerase. pcDNA3-EGFP-Cdc42(Q61L) were purchased from Addgene (plasmid # 12601) [72]. Fragments of Cdc42(Q61L) were amplified from pcDNA3-EGFP-Cdc42(Q61L) and subcloned into pET28a (+) vectors.

Three-dimensional protein structure predictions

The prediction of the three-dimensional structure of the CIP4-HR1 domain was described in Chapter 2.

CD spectroscopy

CD spectra were recorded using a JASCO J-805 spectropolarimeter (JASCO Corporation, Tokyo, Japan) equipped with 1.0 mL quartz cuvettes having a 5-mm path length. The purified HR1 domain was appropriately diluted with 1×PBS to achieve a final concentration of 0.2 mg/mL. Spectral measurements were conducted at 25 °C, covering the 280–198 nm range with a data point interval of 0.2 nm. The acquired spectra were analyzed utilizing the Spectra Manager software (ver 1.0, JASCO Corporation), and the reference spectra were graciously provided by Dr. Yang, J.T [93].

Gel-filtration chromatography

To perform gel-filtration chromatography, I utilized the AKTA purifier system (GE Healthcare, Chicago, IL, USA) under the control of Unicorn 5.1 software (GE Healthcare). The running buffer consisted of 20 mM NaCl, 25 mM HEPES, and 0.2 mM 2-mercaptoethanol. A Superdex 75 10/300 GL column (Cytiva) with a void volume (V_o) of 7.2 mL was applied. To generate the calibration curve, I plotted the partition coefficient (K_{av}) against the molecular weight of the marker proteins. The K_{av} value was calculated using the equation: $K_{av} = (V_e-V_o) / (V_t-V_o)$, where V_e represents the elution volume, V_o represents the void volume, and V_t represents the total volume.

Crosslinking assay

BS^3 crosslinkers (Thermo Fisher Scientific) were dissolved in distilled water and added to the protein solution to a final concentration of 2 mM. The mixture was then incubated at 28 ℃ for 30 minutes. Subsequently, the crosslinker-treated recombinant CIP4-HR1 was analyzed using SDS-PAGE and subjected to silver staining using the Silver Stain II Kit (Fujifilm) following the manufacturer's instructions.

Phase separation assay

In vitro purified and hexa-histidine-tagged CIP4-FDR and Synd2-IDR were used for phase separation assay. The purified proteins were adjusted to the concentration of ~10 mg/mL and incubated with ATTO488-maleimide (Thermo Fisher Scientific) at 28 °C for 1 hour. The reaction was subsequently quenched using 4 mM DTT. To induce droplet formation, 5% polyethylene glycol was added, and the samples were imaged using fluorescence microscopy (FV3000, Olympus Corporation).

To investigate the interaction with actin, purified actin and rhodamine-labelled actin were purchased from Cytoskeleton Inc. (Denver, CO, USA) and reconstituted using the reconstitution buffer (5 mM Tris-HCl (pH 8.0), 0.2 mM CaCl2, 0.2 mM ATP, and 5% (w/v) sucrose). Rhodamine-labelled and non-labelled actin were mixed at a 1:20 ratio to a final concentration of 450 μg/mL, and pre-incubated with Mg^{2+} (50 μM) and EDTA (0.2 mM) at 28 °C for 4 minutes. Purified CIP4-IDR was diluted to 3 mg/mL using the dilution buffer (5 mM Tris-HCl (pH 8.0), 1.2 mM ATP, 1.1 mM DTT, 50 mM KCl, 2 mM $MgCl_2$, and 5% (w/v) polyethylene glycol (Sigma-Aldrich)). The Mg^{2+}-charged actin was then added to a concentration of 45 μg/mL and observed by fluorescence microscopy.

Expression and purification of recombinant proteins

Detailed procedures for protein induction and purification have been describe in Chapter 2.

Turbidity assay

The following recombinant proteins were used in the turbidity assay: hexa-histidine-

tagged FL CIP4, CIP4-FDR, WT Cdc42, Cdc42 (Q61L), N-WASP, bovine serum albumin (BSA, Nacalai Tesque, Inc.), CIP4-FDR, FBP17-FDR, Synd2-IDR, CIP4-FDR-4S, CIP4-HR1, CIP4-HR1(4S), CIP4-FDR(ΔHR1), CIP4-FDR(ΔIDR1) and CIP4-FDR(ΔIDR2). The purified proteins were subjected to serial dilution using the dilution buffer consisting of 50 mM HEPES pH 7.4 and 100 mM NaCl. Each dilution was mixed with an equal volume of droplet buffer containing 30% polyethylene glycol, 50 mM HEPES, 100 mM NaCl at pH 8.0. The mixture was then incubated at 25 °C for 10 minutes and transferred to a micro-cuvette (BRANDTech Scientific Inc., ESSEX, CT, USA), and to measure the optical density at 600 nm by a spectrophotometer (JASCO V-630). The saturation concentration (C_{sat}) was calculated by fitting the obtained data to the following equation using OriginPro (v.9.8): $OD_{600} = OD_{max}\, C^n / (C_{sat}^n + C^n)$, C: protein concentration.

Cell culture and transfection

Procedures for culturing and transfecting Cos7 cells have been described in Chapter 2.

Live-cell fluorescence microscopy

Detailed procedures of live-cell fluorescence microscopy have been described in Chapter 2.

HS-AFM imaging

Detailed procedures of HS-AFM imaging and image analysis have been described in Chapter 2.

Chapter 4. Discussion and Conclusion

4.1 Structural and functional diversity of F-BAR domain-containing proteins

Amino acid sequences with defined 3-dimensional structures and binding partners were initially believed to be the primary determinant of cellular functions or proteins. However, proteomic analysis revealed that more than 30% of the eukaryotic proteins contain short amino acid motifs or long amino acid chains that lack a stable tertiary structure in physiological conditions and were termed 'intrinsically disordered' [94, 95]. Accumulating evidence emphasises the underestimated role of disordered regions in regulating the functions of structured domains and providing docking sites for multiple binding partners [95]. Interestingly, many proteins involved in membrane trafficking, especially CME, contain long stretches of IDRs, including the F-BAR domain-containing proteins [96–98].

CIP4, FBP17, Synd2, and Toca1 are classic members of F-BAR domain-containing proteins [52]. Despite sharing similar domain structures, they exhibited distinct cellular functions and assembled at different timings during CME, which can be attributed, at least in part, to the differences in the curvature of their F-BAR domains [52, 63]. In this study, I provide evidence for the differential self-assembly properties of the middle IDR or FDR between the BAR and SH3 domains. Specifically, I found that the FDRs of CIP4 and FBP17 display a high propensity for LLPS, while the IDR of Synd2 does not exhibit this behaviour (Figure 3-2B and C). Further, both disordered regions are necessary for the phase separation of CIP4-FDR (Figure 3-2E). Notably, even when either of the disordered regions is deleted (ΔIDR1 or ΔIDR2), a certain degree of LLPS propensity is retained (Figure 3-2E). When the dimerization of HR1 was disrupted (4S mutant) (Figure 3-1C), the LLPS propensity was drastically reduced (Figure 3-2E), indicating that HR1 may also contribute to the LLPS of FDR by dimerization. Together, these results provide a clear explanation for the functional diversity observed among Synd2, CIP4, and FBP17 in CME and potentially shed light on other cellular processes involving these proteins.

FBP17, on the contrary, exhibits a charge distribution pattern in its FDR similar to that of CIP4-FDR and displays a comparable phase behaviour *in vitro* (Figure 3-2A–C). However, despite these similarities, they significantly differ in their functions and subcellular localizations. During CME, CIP4 assembles at the CCP earlier than FBP17 (Figure 2-4G). Furthermore, *in vitro* pull-down assay revealed that CIP4-FDR possesses a higher ability for binding to Cdc42 than the FBP17-FDR (Figure 2-10A), suggesting that the disordered regions mediate Cdc42 interactions. Notably, FBP17 exhibits a distinct intracellular distribution from CIP4 in dendritic neurons, likely due to a poly PxxP region within its first IDR [99]. These findings suggest that disordered regions play critical roles in regulating the cellular functions of disordered proteins.

4.2 CIP4 drives the asymmetric actin polymerization and CCP closing

Based on the findings in this study, I propose a model to explain how CIP4 drives the asymmetric CCP closing. When the CCP is absent, CIP4 is recruited by membrane-bound activated Cdc42 via its HR1 domain (Figure 4A). Further, CIP4 recruits N-WASP through its SH3 domain, facilitating the interplay between N-WASP and Cdc42 (Figure 4B). This interaction leads to the formation of ternary complexes involving CIP4, N-WASP, and Cdc42 (Figure 8B). Occasionally, when the ternary complex coincides with the CCP, the BAR domain of CIP4 detects the curved membrane structure of the pit and binds to it (Figure 4C). Through the multimerization of the BAR domain on the membrane, the assembly of CIP4 near the CCP is expedited (Figure 4D). Once the nucleation site of CIP4 was established at CCP, it undergoes ‘charge block-driven LLPS’ via FDR and discontinuously condensates, which drives the ‘asymmetric’ assembly of CIP4 (Figure 4D).

Self-assembly of CIP4 is tightly followed by the recruitment of additional proteins into the CIP4-rich condensates near the CCP (Figuer 4D). The GBD domain of N-WASP exhibited a stronger affinity to Cdc42 than the HR1 domain, resulting in the handover of

Cdc42 from CIP4 to N-WASP and the further recruitment and activation of the Arp2/3 complex [60]. In this study, I found that N-WASP exhibits a high propensity for LLPS and co-separates with CIP4 *in vitro* (Figure 4B), suggesting that the CIP4 condensate is a platform for recruiting and accommodating actin nucleators. Consequently, the local concentration of the active Arp2/3 complex increases, which greatly accelerates actin polymerization (Figure 4E).

Interestingly, actin-associated proteins with long IDRs, such as vasodilator-stimulated phosphoprotein and actin-binding LIM protein 1, were recently reported to form liquid droplets under physiological conditions to promote actin polymerisation and bundling [100, 101]. In line with these observations, our *in vitro* assay demonstrated that G-actin prefers localising within the condensed phase of CIP4-FDR (Figure 3-4C). This suggests that the condensed phase of CIP4 concentrates the local free G-actin and promotes actin polymerization around the CCP.

Inhibition of the Arp2/3-mediated actin polymerization severely inhibited the membrane bulge formation (Figure 2-2A and 2-3C). Therefore, it is reasonable to propose that the mechanical force responsible for the asymmetric deforming of the plasma membrane is generated by 'branched actin' rather than the CIP4 condensates. Previous electron microscopic observations revealed that the branched actin fibres in the vicinity of the CCP exhibit a highly anisotropic nature [51], suggesting that the actin fibres expand radially and exert pressure on the adjacent membrane, resulting in an upward bulge and lateral fusion of the membrane (Figure 4E). It is also plausible that this process generates a downward force, pushing the CCP towards the cell's interior, as proposed by another research group [102]. However, further investigations are warranted to elucidate these phenomena' underlying mechanisms.

4.3 Summary and future perspectives of this study

In this study, I combined live-cell imaging techniques with biophysical and biochemical approaches to elucidate the essential role of the F-BAR domain-containing protein CIP4 in the actin-dependent asymmetric pit-closing in CME. CIP4 interacts with curved membranes and actin-related proteins, such as Cdc42 and N-WASP, through its structured domains, including the F-BAR, HR1, and SH3. Our findings revealed that the self-assembly of the disordered regions between these structured domains facilitates the generation of asymmetricity during this process. This highlights how a multi-domain protein like CIP4 spatio-temporally recruits and orchestrates the actin machinery at specific cellular locations. Moreover, the robust self-assembly and phase separation of the FDR further concentrates the local G-actin and actin-regulatory proteins. It creates an actin-enriched microenvironment neat the CCP before its complete closing.

It has been postulated that unstructured amino acid chains, influenced by their length and net charge, can sense the curved lipid bilayer through entropic or electrostatic mechanisms [103]. Recently, increasing attention has been directed towards disordered proteins that were bound to, anchored to or embedded in the plasma membrane, such as AP180, Amphiphysin 1, FBP17, CALM, and Epsin, as they are believed to support or enhance the membrane-bending capabilities or curvature-sensing properties of structured domains [92, 104–107]. In this research, observations and comparison of the dynamics of chimeric molecules (SCC, SC, and CS, Figure 3-2C–F) at CCP suggested that the F-BAR domains are likely to be functionally exchangeable and that curvature sensing by the BAR domain may not be crucial during the initial stage of endocytic protein assembly. Instead, it implies that the role of the IDR becomes more significant. Hence, our discoveries offer a fresh perspective on the contributions of disordered proteins to the clathrin-mediated endocytic machinery.

A recent study revealed that CIP4 is enriched at the site of artificially-induced nano-scale membrane invaginations, induces actin polymerization in a Cdc42-dependent pathway

[108], and that disordered proteins were proven to sense the membrane curvature outside the area of endocytosis, such as in filopodia [92]. Therefore, it is reasonable to believe that the reorganization of the actin cytoskeleton through F-BAR domain proteins plays a critical role in various cellular structures of the curved membrane, and this should be further elucidated.

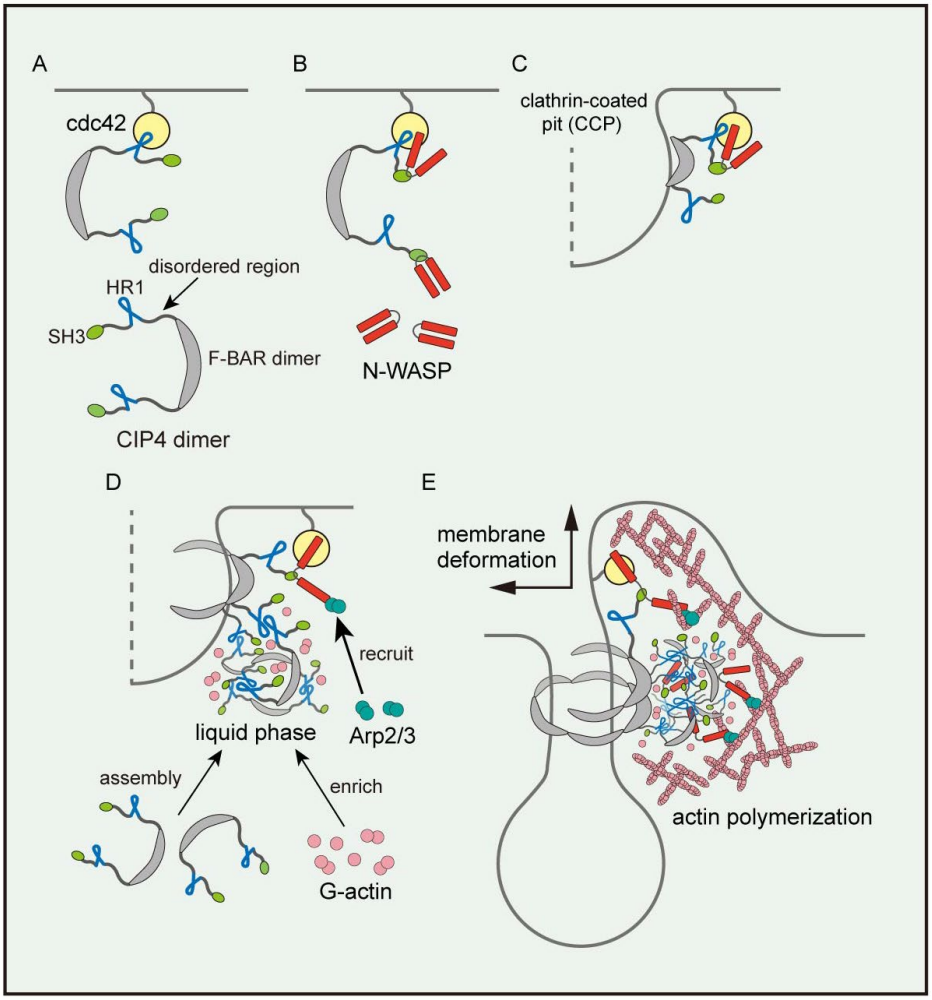

Figure 4. CIP4 drives the asymmetric pit-closing.

A–E, Schematic illustrations of the asymmetric CCP closing induced by CIP4. CIP4 is recruited by membrane-bound and activated Cdc42 via the HR1 domain (A). CIP4 further recruits N-WASP to the CCP. N-WASP binds to Cdc42 and is activated. Therefore, ternary complex forms among CIP4, N-WASP, and Cdc42 (B). When the CCP forms near the ternary complex, the F-BAR domain of CIP4 recognises and binds to the curved membrane (C). Upon the interaction between the F-BAR domain and membrane, the chance of interaction between FDRs increases, which initiates phase separation and asymmetric assembly of CIP4 (D). Simultaneously, the activated N-WASP further recruits and activates the Arp2/3 complex, initiating actin polymerization (D). G-actin is concentrated within the condensed phase of CIP4-FDR, promoting localized actin polymerization and establishing an actin-rich environment (D). Activated N-WASP co-separates with CIP4 around the CCP, accelerating Arp2/3 recruitment (D). Consequently, rapid and asymmetric accumulation of polymerized actin occurs around the CCP, leading to membrane deformation and promoting complete closure of the CCP (E). The clathrin coat is not illustrated in this model.

References

1. Anderson, R. G., Brown, M. S. & Goldstein, J. L. Role of the coated endocytic vesicle in the uptake of receptor-bound low density lipoprotein in human fibroblasts. *Cell* **10**, 351–364 (1977).

2. Rappoport, J. Z. & Simon, S. M. Real-time analysis of clathrin-mediated endocytosis during cell migration. *J. Cell Sci.* **116**, 847–855 (2003).

3. Vieira, A. V., Lamaze, C. & Schmid, S. L. Control of EGF receptor signaling by clathrin-mediated endocytosis. *Science* **274**, 2086–2089 (1996).

4. Chao, W. T., & Kunz, J. Focal adhesion disassembly requires clathrin-dependent endocytosis of integrins. *FEBS Lett.* **583**, 1337–1343 (2009).

5. Kaksonen, M., & Roux, A. Mechanisms of clathrin-mediated endocytosis. *Nat. Rev. Mol. Cell. Biol.* **19**, 313–326 (2018).

6. Kirchhausen, T. Imaging endocytic clathrin structures in living cells. *Trends Cell Biol.* **19**, 596–605 (2009).

7. Kukulski, W., Schorb, M., Kaksonen, M., & Briggs, J. A. Plasma membrane reshaping during endocytosis is revealed by time-resolved electron tomography. *Cell* **150**, 508–520 (2012).

8. Aghamohammadzadeh, S., & Ayscough, K. R. Differential requirements for actin during yeast and mammalian endocytosis. *Nat. Cell. Biol.* **11**, 1039–1042 (2009).

9. Dmitrieff, S., & Nédélec, F. Membrane mechanics of endocytosis in cells with turgor. *PLoS Comput. Biol.* **11**, e1004538 (2015).

10. Tang, H. Y., Xu, J., & Cai, M. Pan1p, End3p, and Sla1p, three yeast proteins required for normal cortical actin cytoskeleton organization, associate with each other and play essential roles in cell wall morphogenesis. *Mol. Cell. Biol.* **20**, 12–25 (2000).

11. Zeng, G., Yu, X., & Cai, M. Regulation of yeast actin cytoskeleton-regulatory complex Pan1p/Sla1p/End3p by serine/threonine kinase Prk1p. *Mol. Cell. Biol.* **12**, 3759–3772 (2001).

12. Merrifield, C. J., & Kaksonen, M. Endocytic accessory factors and regulation of clathrin-mediated endocytosis. *Cold Spring Harb Perspect. Biol.* **6**, a016733 (2014).

13. Zaccai, N. R. *et al*. FCHO controls AP2's initiating role in endocytosis through a PtdIns(4,5)P_2-dependent switch. *Sci. Adv.* **8**, eabn2018 (2022).

14. Day, K. J. *et al.* Liquid-like protein interactions catalyse assembly of endocytic vesicles. *Nat. Cell Biol.* **23**, 366–376 (2021).

15. Lehmann, M. *et al.* Nanoscale coupling of endocytic pit growth and stability. *Sci. Adv.* **5**, eaax5775 (2019).

16. Kadlecova, Z. *et al.* Regulation of clathrin-mediated endocytosis by hierarchical allosteric activation of AP2. *J. Cell Biol.* **216**, 167–179 (2017).

17. Henne, W. M. *et al.* FCHo proteins are nucleators of clathrin-mediated endocytosis. *Science* **328**, 1281–1284 (2010).

18. Yamabhai, M. *et al.* Intersectin, a novel adaptor protein with two Eps15 homology and five Src homology 3 domains. *J. Biol. Chem.* **273**, 31401–31407 (1998).

19. Henne, W. M. *et al.* Structure and analysis of FCHo2 F-BAR domain: a dimerizing and membrane recruitment module that effects membrane curvature. *Structure* **15**, 839–852 (2007).

20. Benmerah, A. *et al.* AP-2/Eps15 interaction is required for receptor-mediated endocytosis. *J Cell Biol.* **140**, 1055–1062 (1998).

21. Pechstein, A. *et al.* Regulation of synaptic vesicle recycling by complex formation between intersectin 1 and the clathrin adaptor complex AP2. *Proc. Natl Acad. Sci. U. S. A.* **107**, 4206–4211 (2010).

22. Kelly, B. T. *et al.* AP2 controls clathrin polymerization with a membrane-activated switch. *Science* **345**, 459–463 (2014).

23. Kirchhausen, T., & Harrison, S. C. Protein organization in clathrin trimers. *Cell* **23**, 755–761 (1981).

24. Heuser, J. E., & Anderson, R. G. Hypertonic media inhibit receptor-mediated endocytosis by blocking clathrin-coated pit formation. *J. Cell Biol.* **108**, 389–400 (1989).

25. Saleem, M. *et al.* A balance between membrane elasticity and polymerization energy sets the shape of spherical clathrin coats. *Nat. Commun.* **6**, 6249 (2015).

26. Dannhauser, P. N., & Ungewickell, E. J. Reconstitution of clathrin-coated bud and vesicle formation with minimal components. *Nat. Cell Biol.* **14**, 634–639 (2012).

27. Yoshida, A. *et al.* Morphological changes of plasma membrane and protein assembly during clathrin-mediated endocytosis. *PLOS Biol.* **16**, e2004786 (2018).

28. Avinoam, O., Schorb, M., Beese, C. J., Briggs, J. A., & Kaksonen, M. Endocytic sites mature by continuous bending and remodeling of the clathrin coat. *Science* **348**, 1369–1372 (2015).

29. Mund, M. *et al.* Clathrin coats partially preassemble and subsequently bend during endocytosis. *J. Cell Biol.* **222**, e202206038 (2023).

30. Hinshaw, J. E. & Schmid, S. L. Dynamin self-assembles into rings suggesting a mechanism for coated vesicle budding. *Nature* **374**, 190–192 (1995).

31. Shnyrova, A. V. *et al.* Geometric catalysis of membrane fission driven by flexible dynamin rings. *Science* **339**, 1433–1436 (2013).

32. Antonny, B. *et al.* Membrane fission by dynamin: what we know and what we need to know. *EMBO J.* **35**, 2270–2284 (2016).

33. Braell, W. A., Schlossman, D. M., Schmid, S. L., & Rothman, J. E. Dissociation of

clathrin coats coupled to the hydrolysis of ATP: role of an uncoating ATPase. *J. Cell Biol.* **99**, 734–741 (1984).

34. Schlossman, D. M., Schmid, S. L., Braell, W. A., & Rothman, J. E. An enzyme that removes clathrin coats: purification of an uncoating ATPase *J. Cell Biol.* **99**, 723–733 (1984).

35. Eisenberg, E., & Greene, L. E. Multiple roles of auxilin and hsc70 in clathrin-mediated endocytosis. *Traffic* **8**, 640–646 (2007).

36. Sousa, R. *et al.* Clathrin-coat disassembly illuminates the mechanisms of Hsp70 force generation. *Nat. Struct. Mol. Biol.* **23**, 821–829 (2016).

37. Cremona, O. *et al.* Essential role of phosphoinositide metabolism in synaptic vesicle recycling. *Cell* **99**, 179–188 (1999).

38. Verstreken, P. *et al.* Endophilin mutations block clathrin-mediated endocytosis but not neurotransmitter release. *Cell* **109**, 101–112 (2002).

39. Verstreken, P. *et al.* Synaptojanin is recruited by endophilin to promote synaptic vesicle uncoating. *Neuron* **40**, 733–748 (2003).

40. Arasada, R., Sayyad, W. A., Berro, J., & Pollard, T. D. High-speed superresolution imaging of the proteins in fission yeast clathrin-mediated endocytic actin patches. *Mol. Biol. Cell* **29**, 295–303 (2018).

41. Huang, B., Wang, W., Bates, M., & Zhuang, X. Three-dimensional super-resolution imaging by stochastic optical reconstruction microscopy. *Science* **319**, 810–813 (2008).

42. Jones, S. A., Shim, S. H., He, J., & Zhuang, X. Fast, three-dimensional super-resolution imaging of live cells. *Nat. Methods* **8**, 499–505 (2011).

43. Merrifield, C. J., Perrais, D., & Zenisek, D. Coupling between clathrin-coated-pit invagination, cortactin recruitment, and membrane scission observed in live cells. *Cell* **121**, 593–606 (2005).

44. Yu, Y., & Yoshimura, S. H. Investigating the morphological dynamics of the plasma membrane by high-speed atomic force microscopy. *J. Cell Sci.* **134**, jcs243584 (2021).

45. Suzuki, Y. *et al.* High-speed atomic force microscopy combined with inverted optical microscopy for studying cellular events. *Sci. Rep.* **3**, 2131 (2013).

46. Yoshida, A. *et al.* Probing in vivo dynamics of mitochondria and cortical actin networks using high-speed atomic force/fluorescence microscopy. *Genes Cells* **20**, 85-94 (2015).

47. Higgins, M. K., & McMahon, H. T. Snap-shots of clathrin-mediated endocytosis. *Trends Biochem. Sci.* **27**, 257–263 (2002).

48. Ferguson, S. *et al.* Coordinated actions of actin and BAR proteins upstream of dynamin at endocytic clathrin-coated pits. *Dev. Cell* **17**, 811–822 (2009).

49. Hinshaw, J. E. Dynamin and its role in membrane fission. Annu. Rev. *Cell Dev. Biol.* **16**, 483–519 (2000).

50. Shevchuk, A. I. *et al.* An alternative mechanism of clathrin-coated pit closure revealed by ion conductance microscopy. *J. Cell Biol.* **197**, 499–508 (2012).

51. Collins, A., Warrington, A., Taylor, K. A., & Svitkina, T. Structural organization of the actin cytoskeleton at sites of clathrin-mediated endocytosis. *Curr. Biol.* **21**, 1167-1175 (2011).

52. Qualmann, B., Koch, D., & Kessels, M. M. Let's go bananas: revisiting the endocytic BAR code. *EMBO J.* **30**, 3501–3515 (2011).

53. Peter, B. J. *et al.* BAR domains as sensors of membrane curvature: the amphiphysin BAR structure. *Science* **303**, 495–499 (2004).

54. Farsad, K. *et al.* Generation of high curvature membranes mediated by direct endophilin bilayer interactions. *J. Cell Biol.* **155**, 193–200 (2001).

55. Takei, K., Slepnev, V. I., Haucke, V., & De Camilli, P. (1999). Functional partnership between amphiphysin and dynamin in clathrin-mediated endocytosis. *Nat. Cell Biol.* **1**, 33–

39.

56. Ayton, G. S., Blood, P. D., & Voth, G. A. Membrane remodeling from N-BAR domain interactions: insights from multi-scale simulation. *Biophys. J.* **92**, 3595–3602 (2007).

57. Chial, H. J. *et al.* Membrane targeting by APPL1 and APPL2: dynamic scaffolds that oligomerize and bind phosphoinositides. *Traffic* **9**, 215–229 (2008).

58. Kessels, M. M., & Qualmann, B. Syndapin oligomers interconnect the machineries for endocytic vesicle formation and actin polymerization. *J. Biol. Chem.* **281**, 13285–13299 (2006).

59. Shimada, A. *et al.* Curved EFC/F-BAR-domain dimers are joined end to end into a filament for membrane invagination in endocytosis. *Cell* **129**, 761–772 (2007).

60. Watson, J. R. *et al.* Investigation of the interaction between Cdc42 and its effector TOCA1: handover of Cdc42 to the actin regulator N-WASP is facilitated by differential binding affinities. *J. Biol. Chem.* **291**, 13875–13890 (2016).

61. Ho, H. Y. H. *et al.* Toca-1 mediates Cdc42-dependent actin nucleation by activating the N-WASP-WIP complex. *Cell* **118**, 203–216 (2004).

62. Kostan, J. et al. Direct interaction of actin filaments with F-BAR protein pacsin2. *EMBO Rep.* **15**, 1154–1162 (2014).

63. Armstrong, G., & Olson, M. F. Bending over backwards: BAR proteins and the actin cytoskeleton in mammalian receptor-mediated endocytosis. *Eur. J. Cell Biol.* **101**, 151257 (2022).

64. Aspenström, P. Roles of F-BAR/PCH proteins in the regulation of membrane dynamics and actin reorganization. *Int. Rev. Cell Mol. Biol.* **272**, 1–31 (2009).

65. Taylor, M. J., Perrais, D. & Merrifield, C. J. A high precision survey of the molecular dynamics of mammalian clathrin-mediated endocytosis. *PLOS Biol.* **9**, e1000604 (2011).

66. Fricke, R. *et al.* Drosophila Cip4/Toca-1 integrates membrane trafficking and actin dynamics through WASP and SCAR/WAVE. *Curr. Biol.* **19**, 1429–1437 (2009).

67. Prehoda, K. E., Scott, J. A., Mullins, R. D. & Lim, W. A. Integration of multiple signals through cooperative regulation of the N-WASP-Arp2/3 complex. *Science* **290**, 801–806 (2000).

68. Aspenström, P. A Cdc42 target protein with homology to the non-kinase domain of FER has a potential role in regulating the actin cytoskeleton. *Curr. Biol.* **7**, 479–487 (1997).

69. Vasan, R., Rudraraju, S., Akamatsu, M., Garikipati, K., & Rangamani, P. A mechanical model reveals that non-axisymmetric buckling lowers the energy barrier associated with membrane neck constriction. *Soft Matter* **16**, 784–797 (2020).

70. Jin, M. *et al.* Branched actin networks are organized for asymmetric force production during clathrin-mediated endocytosis in mammalian cells. *Nat. Commun.* **13**, 3578 (2022).

71. Römer, W. *et al.* Actin dynamics drive membrane reorganization and scission in clathrin-independent endocytosis. *Cell* **140**, 540–553 (2010).

72. Nalbant, P., Hodgson, L., Kraynov, V., Toutchkine, A. & Hahn, K. M. Activation of endogenous Cdc42 visualized in living cells. *Science* **305**, 1615–1619 (2004).

73. Ma, L., Cantley, L. C., Janmey, P. A. & Kirschner, M. W. Corequirement of specific phosphoinositides and small GTP-binding protein Cdc42 in inducing actin assembly in Xenopus egg extracts. *J. Cell Biol.* **140**, 1125–1136 (1998).

74. Erdős, G., Pajkos, M., & Dosztányi, Z. IUPred3: prediction of protein disorder enhanced with unambiguous experimental annotation and visualization of evolutionary conservation. *Nucleic Acids Res.* **49**, W297–W303 (2021).

75. Notredame, C., Higgins, D. G., & Heringa, J. T-Coffee: A novel method for fast and accurate multiple sequence alignment. *J. Mol. Biol.* **302**, 205–217 (2000).

76. Jumper, J. *et al.* Highly accurate protein structure prediction with AlphaFold. *Nature* **596**, 583–589 (2021).

77. Mirdita, M. *et al.* ColabFold: making protein folding accessible to all. *Nat. Methods* **19**, 679–682 (2022).

78. Sochacki, K. A., Dickey, A. M., Strub, M. P. & Taraska, J. W. Endocytic proteins are partitioned at the edge of the clathrin lattice in mammalian cells. *Nat. Cell Biol.* **19**, 352–361 (2017).

79. Fujimoto, L. M., Roth, R., Heuser, J. E., & Schmid, S. L. Actin assembly plays a variable, but not obligatory role in receptor-mediated endocytosis. *Traffic* **1**, 161–171 (2000).

80. Yarar, D., Waterman-Storer, C. M., & Schmid, S. L. A dynamic actin cytoskeleton functions at multiple stages of clathrin-mediated endocytosis. *Mol. Biol. Cell* **16**, 964–975 (2005).

81. Lamaze, C., Fujimoto, L. M., Yin, H. L., & Schmid, S. L. The actin cytoskeleton is required for receptor-mediated endocytosis in mammalian cells. *J. Biol. Chem.* **272**, 20332–20335 (1997).

82. Boulant, S., Kural, C., Zeeh, J. C., Ubelmann, F., & Kirchhausen, T. Actin dynamics counteract membrane tension during clathrin-mediated endocytosis. *Nat. Cell. Biol.* **13**, 1124–1131 (2011).

83. Pollard, T. D., & Borisy, G. G. Cellular motility driven by assembly and disassembly of actin filaments. *Cell* **112**, 453–465 (2003).

84. Tsujita, K. *et al.* Coordination between the actin cytoskeleton and membrane deformation by a novel membrane tubulation domain of PCH proteins is involved in endocytosis. *J. Cell Biol.* **172**, 269-279 (2006).

85. Grassart, A. *et al.* Actin and dynamin2 dynamics and interplay during clathrin-mediated

endocytosis. *J. Cell Biol.* **205**, 721–735 (2014).

86. Zhang, R. *et al.* Dynamin regulates the dynamics and mechanical strength of the actin cytoskeleton as a multifilament actin-bundling protein. *Nat. Cell Biol.* **22**, 674–688 (2020).

87. Yamazaki, H., Takagi, M., Kosako, H., Hirano, T. & Yoshimura, S. H. Cell cycle-specific phase separation regulated by protein charge blockiness. *Nat. Cell Biol.* **24**, 625–632 (2022).

88. Lin, Y. H., Forman-Kay, J. D. & Chan, H. S. Sequence-specific polyampholyte phase separation in membraneless organelles. *Phys. Rev. Lett.* **117**, 178101 (2016).

89. Lyons, H. *et al.* Functional partitioning of transcriptional regulators by patterned charge blocks. *Cell* **186**, 327–345.e28 (2023).

90. Ditlev, J. A. Membrane-associated phase separation: organization and function emerge from a two-dimensional milieu. *J. Mol. Cell Biol.* **13**, 319–324 (2021).

91. Zhao, Y. G. & Zhang, H. Phase separation in membrane biology: the interplay between membrane-bound organelles and membraneless condensates. *Dev. Cell* **55**, 30–44 (2020).

92. Zeno, W. F. *et al.* Synergy between intrinsically disordered domains and structured proteins amplifies membrane curvature sensing. *Nat. Commun.* **9**, 4152 (2018).

93. Yang, J. T., Wu, C. S. C. & Martinez, H. M. Calculation of protein conformation from circular dichroism. *Methods Enzymol.* **130**, 208–269 (1986).

94. Pentony, M. M., & Jones, D. T. Modularity of intrinsic disorder in the human proteome. *Proteins* **78**, 212–221 (2010).

95. Dyson, H. J., & Wright, P. E. Intrinsically unstructured proteins and their functions. *Nat. Rev. Mol. Cell Biol.* **6**, 197–208 (2005).

96. Van Der Lee, R. et al. Classification of intrinsically disordered regions and proteins. *Chem. Rev.* **114**, 6589–6631 (2014).

97. Schmid, E. M., & McMahon, H. T. Integrating molecular and network biology to decode endocytosis. *Nature* **448**, 883–888 (2007).

98. Pietrosemoli, N., Pancsa, R., & Tompa, P. Structural disorder provides increased adaptability for vesicle trafficking pathways. *PLoS Comput. Biol.* **9**, e1003144 (2013).

99. Taylor, K. L. *et al.* Opposing functions of F-BAR proteins in neuronal membrane protrusion, tubule formation, and neurite outgrowth. *Life Sci. Alliance* **2**, e201800288 (2019).

100. Graham, K. *et al.* Liquid-like VASP condensates drive actin polymerization and dynamic bundling. *Nat. Phys.* **19**, 574–585 (2023).

101. Yang, S. *et al.* Self-construction of actin networks through phase separation–induced abLIM1 condensates. *Proc. Natl Acad. Sci. U. S. A.* **119**, e2122420119 (2022).

102. Akamatsu, M. *et al.* Principles of self-organization and load adaptation by the actin cytoskeleton during clathrin-mediated endocytosis. *eLife* **9**, e49840 (2020).

103. Zeno, W. F. *et al.* Molecular mechanisms of membrane curvature sensing by a disordered protein. *J. Am. Chem. Soc.* **141**, 10361–10371 (2019).

104. Su, M. *et al.* Comparative study of curvature sensing mediated by F-BAR and an intrinsically disordered region of FBP17. *iScience* **23**, 101712 (2020).

105. Zeno, W. F., Snead, W. T., Thatte, A. S. & Stachowiak, J. C. Structured and intrinsically disordered domains within Amphiphysin1 work together to sense and drive membrane curvature. *Soft Matter* **15**, 8706–8717 (2019).

106. Stahelin, R. V. *et al.* Contrasting membrane interaction mechanisms of AP180 N-terminal homology (ANTH) and epsin N-terminal homology (ENTH) domains. *J. Biol. Chem.* **278**, 28993–28999 (2003).

107. Miller, S. E. *et al.* CALM regulates clathrin-coated vesicle size and maturation by directly sensing and driving membrane curvature. *Dev. Cell* **33**, 163–175 (2015).

108. Ledoux, B. *et al.* Plasma membrane nanodeformations promote actin polymerisation through 807 CIP4/CDC42 recruitment and regulate type II IFN signaling. *bioRxiv.* 10.1101/2022.08.16.504113 (2022).

This thesis is based on material contained in the following scholarly paper(s).

1. Yu, Y. & Yoshimura, S. H. Self-assembly of CIP4 drives actin-mediated asymmetric pit-closing in clathrin-mediated endocytosis. *Nat. Commun.* **14**, 4602 (2023).

2. Yu, Y., & Yoshimura, S. H. Investigating the morphological dynamics of the plasma membrane by high-speed atomic force microscopy. *J. Cell Sci.* **134**, jcs243584 (2021).